A MULTI-WAVELENGTH SPECTRAL AND POLARIMETRIC STUDY OF THE JET OF 3C 264

E. S. PERLMAN[1,2], C. A. PADGETT[2,3], M. GEORGANOPOULOS[2,3], D. M. WORRALL[4], J. H. KASTNER[5], G. FRANZ[5], M. BIRKINSHAW[4], F. DULWICH[4], C. P. O'DEA[5], S. A. BAUM[6], W. B. SPARKS[7], J. A. BIRETTA[7], L. LARA[8,10], S. JESTER[9], AND A. MARTEL[7]

[1] Physics and Space Sciences Department, Florida Institute of Technology, 150 West University Boulevard, Melbourne, FL 32901, USA; eperlman@fit.edu
[2] Department of Physics, University of Maryland-Baltimore County, 1000 Hilltop Circle, Baltimore, MD 21250, USA
[3] NASA's Goddard Space Flight Center, Mail Code 660, Greenbelt, MD 20771, USA
[4] Department of Physics, University of Bristol, Tyndall Avenue, Bristol BS8 1TL, UK
[5] Physics Department, Rochester Institute of Technology, 84 Lomb Memorial Drive, Rochester, NY 14623-5603, USA
[6] Center for Imaging Science, Rochester Institute of Technology, 54 Lomb Memorial Drive, Rochester, NY 14623-5603, USA
[7] Space Telescope Science Institute, 3700 San Martin Drive, Baltimore, MD 21218, USA
[8] Dpto. Fisíca Teórica y del Cosmos, Universidad de Granada, Avenida Fuentenueva s/n, 18071 Granada, Spain
[9] Max Planck Institut fur Astronomie, Königstuhl 17, D-69117 Heidelberg, Germany

ABSTRACT

We present a comprehensive multi-band spectral and polarimetric study of the jet of 3C 264 (NGC 3862). Included in this study are three *Hubble Space Telescope* (*HST*) optical and ultraviolet polarimetry data sets, along with new and archival Very Large Array radio imaging and polarimetry, a re-analysis of numerous *HST* broadband data sets from the near infrared to the far ultraviolet, and a *Chandra* ACIS-S observation. We investigate similarities and differences between optical and radio polarimetry, in both degree of polarization and projected magnetic field direction. We also examine the broadband spectral energy distribution of both the nucleus and jet of 3C 264, from the radio through the X-rays. From this, we place constraints on the physics of the 3C 264 system, the jet and its dynamics. We find significant curvature of the spectrum from the near-IR to ultraviolet, and synchrotron breaks steeper than 0.5, a situation also encountered in the jet of M87. This likely indicates velocity and/or magnetic field gradients and more efficient particle acceleration localized in the faster/higher magnetic field parts of the flow. The magnetic field structure of the 3C 264 jet is remarkably smooth; however, we do find complex magnetic field structure that is correlated with changes in the optical spectrum. We find that the X-ray emission is due to the synchrotron process; we model the jet spectrum and discuss mechanisms for accelerating particles to the needed energies, together with implications for the orientation of the jet under a possible spine-sheath model.

Key words: galaxies: active – galaxies: elliptical and lenticular, cD – galaxies: jets – polarization – radiation mechanisms: non-thermal

Online-only material: color figures

1. INTRODUCTION

The characterization of jet polarization properties provides a powerful diagnostic of jet physics, particularly with respect to magnetic field configuration and particle acceleration. Extragalactic jets generally emit a continuum of radiation from radio through optical, and often into the X-ray regime. Through matched resolution comparisons of flux density measurements at various frequencies, we can glean morphological information about particle acceleration regions and jet energetic structure.

The closest kiloparsec-scale radio–optical jet is that of M87 at a distance of 16 Mpc (Tonry 1991). By using matched resolution polarimetry at different wavelengths and combining this with multi-wavelength imaging and X-ray imaging and spectroscopy, much information about jet energetics and magnetic fields, three-dimensional structure and particle acceleration can be constrained (Perlman & Wilson 2005 and references therein). There are relatively few jets for which there exists *Hubble Space Telescope (HST)* optical polarimetry compared to the number that have been detected. As of this writing, a total of 10 optical jets have *HST* polarimetry observations (M87—e.g., Perlman et al. 1999; 3C 273—Thomson et al. 1993; 3C 293—Floyd et al. 2006; 3C 15—Perlman et al. 2006 and Dulwich et al. 2007; 3C 346—Perlman et al. 2006 and Dulwich et al. 2009; 3C 66B, 3C 78, 3C 264, and 3C 371—Perlman et al. 2006;

PKS 1136–135—M. Cara et al. 2010, in preparation). This is in comparison to the ∼34 detected optical extragalactic jets.[11] Given this dearth of polarimetry observations, it is not surprising that there are few constraints on the configuration of the magnetic fields in optically emitting regions of extragalactic jets. Here, we present a comprehensive study of the jet of 3C 264 that includes radio and optical polarimetry, as well as X-ray observations of the jet.

At a redshift of 0.0217 (Baum et al. 1990), and hence a distance of 94 Mpc, 3C 264 is among the closest known bright radio galaxies with an optical jet. Also detected at X-ray energies, its relative proximity makes the 3C 264 jet a prime candidate for deep optical, radio and X-ray studies, as we present here. It is hosted by NGC 3862, a large elliptical galaxy offset to the south–east from the center of the cluster Abell 1367, and is classified as a Fanaroff–Riley type I radio source (Fanaroff & Riley 1974). On large scales, it exhibits a twin-tail radio structure extending to the north–east (Bridle & Vallee 1981). On arcsec scales, it consists of a compact core, with a one-sided, nearly knot-free jet extending also to the north–east and a weak counter jet (Lara et al. 1997). The optical jet counterpart extends for only roughly 2″ beyond the galaxy core, the latter arcsecond of which is considerably fainter than the inner jet (Perlman et al. 2006). This short length combined with the "smoothness" of the jet makes studying this object difficult.

---

[10] Deceased

[11] See http://home.fnal.gov/~jester/optjets/ maintained by S. Jester.

Table 1
HST Observations

Instrument	Filter/Polarizer	λ_0[a]	FWHM[b]	Num Exp[c]	Obs Date	Time (s)[d]
WFPC2/PC	F702W	6919	1382	2	1994 Dec 24	280
WFPC2/PC	F606W	5997	1502	1	1995 Apr 16	500
WFPC2/PC	F791W	7881	1224	2	1996 May 19	750
WFPC2/PC	F547M	5483	484	2	1996 May 19	900
NICMOS/NIC2	F110W	11285	3844	4	1998 May 12	448
NICMOS/NIC2	F160W	16030	2772	4	1998 May 12	448
NICMOS/NIC2	F205W	20714	4314	4	1998 May 12	896
STIS/NUV-MAMA	F25QTZ	2354	995	1	2000 Feb 12	1800
STIS/FUV-MAMA	25MAMA	1374	318	1	2000 Feb 12	1705
STIS/FUV-MAMA	F25SRF2	1469	281	1	2000 Feb 12	1700
WFPC2/PC	F702W	6919	1382	9	2002 Mar 30	1400
ACS/HRC	F606W/POL0V	5895	1588	2	2002 Dec 05	300
ACS/HRC	F606W/POL60V	5895	1588	2	2002 Dec 05	300
ACS/HRC	F606W/POL120V	5895	1588	2	2002 Dec 05	300
ACS/HRC	F330W/POL0UV	3372	410	2	2002 Dec 05	300
ACS/HRC	F330W/POL60UV	3372	410	2	2002 Dec 05	300
ACS/HRC	F330W/POL120UV	3372	410	2	2002 Dec 05	300
WFPC2/PC	F555W/POLQ[e]	5439	1232	8	2003 Mar 06	6500
WFPC2/PC	F555W/POLQ[e]	5439	1232	8	2003 Apr 25	6500
WFPC2/PC	F555W/POLQ[e]	5439	1232	8	2003 Jun 01	6500

Notes.

[a] Pivot wavelength of filter in Å.

[b] Approximate FWHM of filter bandpass in Å.

[c] Number of images in raw data set (including CR-SPLITs).

[d] Total integration time of all images in seconds.

[e] Due to non-rotatability of the WFPC2 polarizer (POLQ), *HST* was allowed to precess between observations over a ∼2 month time period, simulating the nominal polarizer angles of $0°$, $60°$, and $120°$. See the text for details.

In particular, in the optical and near-IR useful observations are really only possible with *HST*, as most adaptive-optics systems require a nearby, bright point source.

3C 264 was part of the original Third Cambridge Catalog with $S_{159\,\mathrm{MHz}} = 37$ Jy (Edge et al. 1959) and the optical jet counterpart was discovered by Crane et al. (1993) with the pre-COSTAR Faint Object Camera (FOC) instrument on *HST*. Since this initial optical discovery, over 50 ks of *HST* observing time has been dedicated to this source alone (e.g., Crane et al. 1993; Baum et al. 1997, 1998; Hutchings et al. 1998; Martel et al. 1999, 2000; Noel-Storr et al. 2003). More recent observations have concentrated on deep optical polarimetry with WFPC2 (Perlman et al. 2006) and optical and UV polarimetry with the *HST* Advanced Camera for Surveys (ACS) (Capetti et al. 2007). It was first detected in X-rays with *Einstein* (Elvis et al. 1981), and more recently observed by *Chandra* and *XMM-Newton*, with the nuclear emissions studied by Donato et al. (2004) and Evans et al. (2006), and the hot atmosphere by Sun et al. (2007). Also, several radio observations have been performed with the Very Large Array (VLA; Lara et al. 1999, 2004; this paper), the global VLBI network (Lara et al. 1997) and the European VLBI network (EVN) and MERLIN arrays (Baum et al. 1997; Lara et al. 1999, 2004).

In this paper, we attempt to bring all of this observational information into a coherent picture of the physics of the 3C 264 jet. In Section 2, we detail the observations and data reduction techniques used. In Section 3, we present comparisons between optical and radio polarimetry, optical and radio spectral index maps, and a comparison of the resolved and unresolved jet emissions from *Chandra*. Lastly, in Section 4, we discuss the implications of these results, and present a simple model that attempts to explain them. Throughout the paper, we assume a flat Friedmann cosmology with $H_0 = 72$ km s^{-1} Mpc^{-1},

(corresponding to the latest *WMAP* cosmology, see Dunkley et al. 2009), giving a projected linear scale of 0.42 kpc arcsec^{-1}.

2. OBSERVATIONS AND DATA REDUCTION

We obtained polarimetric observations of 3C 264 with the WFPC2 instrument aboard *HST* as part of the Cycle 10 observing program GO-9142. As part of this same proposal, we obtained 38.3 ks of *Chandra* observations of this source. We also observed this object with the *VLA* in both A and B configurations at 8.5 GHz and 22.5 GHz as part of observing program AP0439. Further observations in many wave bands and instrument configurations with *HST* have been taken from the online data archives (Table 1). What follows is a discussion of the individual observing programs, as well as the methods used to reduce them.

2.1. HST

We observed 3C 264 in three separate epochs with *HST*'s WFPC2 instrument during an approximately two month time period between March and June of 2003 (see Table 1). We used the wideband F555W filter, combined with the POLQ polarizer. The time separation for these observations was necessary[12] since we wanted the object to reside on the PC chip, and the POLQ filter rotates only through ∼50°. All of the rotated positions leave the PC either severely vignetted or not covered by the same polarizer. Thus, *HST* was allowed to precess between observations so that the polarizer angles approximated the standard $0°$, $60°$, and $120°$ polarizer angles. Windows of $15°$ in

---

[12] To obtain high-quality polarimetry, it is necessary to take observations through three polarizers, with the second and third nominally oriented at either $60°$ and $120°$ or $45°$ and $90°$ with respect to the first.

orientation were allowed for scheduling purposes, and to avoid the jet lying along a diffraction spike, ORIENTs were chosen carefully. The PC chip was chosen due to its higher angular resolution as compared to the WF chips. Sub-pixel dithering was used in order to fully sample the point-spread function (PSF), and hence achieve diffraction-limited *HST* resolution in this wave band.

HST ACS polarimetry was also obtained for 3C 264 as part of GO program 9493, in December of 2002 (Table 1). These observations were taken with the High-Resolution Channel (HRC) of the ACS, combined with the wideband optical F606W filter, and the F330W UV filter. The optical polarimetry was taken through the three visible polarizers aboard ACS, namely POL0V, POL60V, and POL120V, and the UV polarimetry was obtained using the three UV polarizers, namely POL0UV, POL60UV, and POL120UV. The ACS is better suited to polarimetry than WFPC2, in that it has higher sensitivity—more than seven times that of WFPC2 at ~6000 Å (Heyer 2004)—it has three polarizers oriented very near to the ideal polarizer angles, and the PSF is better behaved across the chip. The fact that ACS has three properly oriented polarizers (for both optical and UV) allows the necessary polarization observations to be taken in the same epoch. This simplifies the data reduction process significantly, by easing the image registration process with unrotated PSFs, and eliminating the effects of varying PSFs across the imaging chips, both of which complicated the WFPC2 polarimetry reduction (see Perlman et al. 2006 for details). It also eliminates the possible complication of jet variability. However, the exposure times for these two data sets are much shorter than our WFPC2 polarimetry, hence we are not able to detect jet emission to the same levels, despite the increased sensitivity of ACS.

We also used the online *HST* data archive to obtain imaging observations of 3C 264 in numerous wave bands (see Table 1), allowing us to explore the optical spectrum of the jet. The results cover eight years of observations, at wavelengths from ~1400 Å to 2 μm, and include data from WFPC2, Space Telescope Imaging Spectrograph (STIS) as well as NICMOS.

All of the WFPC2 data were reduced using standard techniques with stsdas in iraf.[13] The images were calibrated using the best dark count images and flat field images available. Cosmic-ray rejection was done using the stsdas task crrej for all but one data set. The F606W image was a single, non-CR-SPLIT observation, and as such, could not have the cosmic rays removed. Fortunately, there were no cosmic-ray events in the jet region, so the cosmic rays were simply masked during galaxy subtraction (see below). The resulting cosmic-ray free images were then *drizzled* on to the native WFPC2/PC pixel scale of 0″0455 pixel^{-1} and converted to counts s^{-1}, using the stsdas task drizzle. This task corrects for the field distortion of WFPC2, for which we used the latest geometric correction coefficients for the PC chip (Anderson & King 2003).

The above steps were also taken for each individual observation through the polarizer, except that these data were subsampled onto half the native PC pixel scale—0″02275 pixel^{-1}. Since our polarimetry observations are quite deep (four orbits in all; nearly 2 hr through each polarizer), we were able to detect jet emission out to nearly 2″ from the core. As we used sub-pixel dithering, we were able to fully sample the PSF on the PC chip and achieve diffraction-limited resolution (Heyer 2004). Similarly to the WFPC2 data, the ACS/HRC data listed

in Table 1 were reprocessed with the best dark count and flat field images available in the archive, using the procedure outlined in Pavlovsky et al. (2005). These data were further reduced using the PyRAF task multidrizzle. In our case, since there is only a single CR-SPLIT observation for each polarizer, this multi-faceted task was limited to cosmic-ray rejection and geometric distortion correction. For the latter, we used the latest geometric distortion coefficients for the HRC (Anderson & King 2004).

The STIS NUV- and FUV-MAMA data listed in Table 1 were calibrated using STScI's On-The-Fly-Reprocessing (OTFR), which uses the best available flat field images and dark count corrections. OTFR also *drizzled* the images onto the native FUV-MAMA and NUV-MAMA pixel scales of 0″0246 × 0″0247 pixel^{-1} and 0″0245 × 0″0248 pixel^{-1}, respectively. The sky background for each image was estimated to be simply the mode of all pixels, using the iraf task imstatistics with two iterations of 3σ rejection. This approach was necessary since there was only a single exposure for each detector. Galaxy subtraction (see below) was only performed for the NUV-MAMA image, since galaxy light is minimal, if present, in the FUV-MAMA images. The STIS data were the only *HST* observations for which sky subtraction was possible, given the large angular size of the host galaxy, which filled the field of the WFPC2, ACS/HRC, and NICMOS data.

The NICMOS data listed in Table 1 were taken with the NIC2 camera, in multiaccum mode. These data were also reprocessed using OTFR, with the best available flat fields and dark count images. For the F205W data, the pipeline flats did not completely account for the NIC2 response at this wavelength and for these particular observations. The spatial scale of the variations is however larger than the extent of the region of interest (i.e. the jet); and we were able to subtract the galaxy to achieve a residual noise level of only 0.026 counts s^{-1} pixel^{-1}. The "pedestal" bias (Dickenson et al. 2004) was removed using the stsdas task pedsub (based on the original code, "unpedestal," by R. van der Marel), which is designed to handle crowded fields. This produced a better reduction of the quadrant bias than did the other commonly used task pedsky. For each of the three filters there were four dithered observations, which were *drizzled* separately onto a common frame with the nominal NIC2 pixel scale of 0″0775 pixel^{-1}. The individually *drizzled* images were then median combined using the iraf task imcombine, rejecting the lowest of the four values at each pixel. This was done to account for the fact that these observations unfortunately placed the jet across the NIC2 erratic middle column (Dickenson et al. 2004), which shows up as a dark strip. Since drizzle is more or less a shift-and-add algorithm, it does not do well with artifacts of this nature. Hence, rejecting the lowest valued pixels seemed the best solution.

Once the calibrated images were made, an isophotal model of the host galaxy was obtained using the iraf tasks ellipse and bmodel (Perlman et al. 1999). The jet and globular clusters were masked out during the isophotal fitting, as their inclusion leads to oversubtracted ring-like artifacts in the subtracted images. In addition to this masking, outlying pixels were excluded using a 3σ rejection in the isophotal fits. The resulting isophotal fit is shown in Figure 1 for the WFPC2 polarization image, compared to the radial profile extracted from the polarization data. As can be seen, the galaxy subtraction process was made difficult by the nearly circular dust "disk" extending out to ~0″8–0″9 from the galaxy core (Martel et al. 1998, 2000), as well as a ring of enhanced emission just outside of this dust disk. To overcome

---

[13] For an introduction to iraf and stsdas, see http://iraf.net and http://www.stsci.edu/resources/software_/hardware/stsdas.
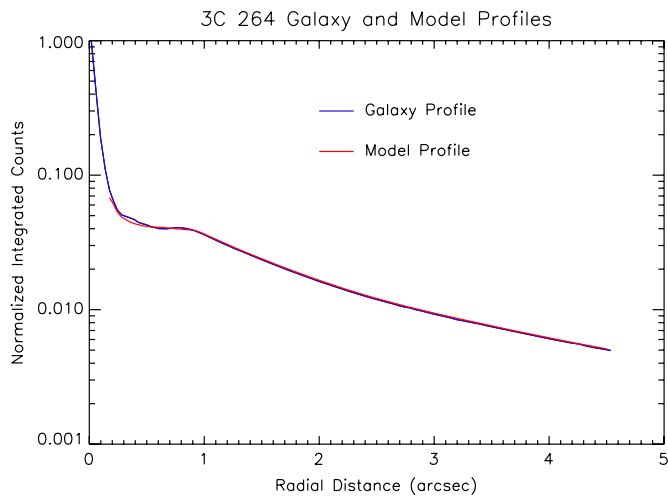
Figure 1. Integrated radial profile of a single polarizer image from WFPC2 plotted with the radial profile of our best-fit isophotal model. The jet emission can be seen between $0\farcs3$ and $1\farcs0$, as slight enhancements in the galaxy profile. Note that the galaxy model does not extend inward of $\sim0\farcs2$ since the core of the WFPC2/PC PSF is not well modeled by ellipses.

(A color version of this figure is available in the online journal.)

this, we interpolated our models linearly over most of the dusty region, including only those isophotes that were well centered on the galaxy core, and very close to circular. The latter criterion was chosen since the galaxy itself is classified as an E0 elliptical, and hence nearly all of its isophotes have ellipticities $\lesssim 0.1$.

After the galaxy light was subtracted, the polarization images were combined to produce Stokes I, Q, and U images, as well as fractional polarization (%P) and polarization position angle (P.A.) images. For the details of this process, see Perlman et al. (2006). The resulting optical polarimetry is shown in Figure 2. For comparison, radio imaging and polarimetry (next section) are shown in Figure 3.

The imaging observations (including the Stokes I images) were resampled onto the WFPC2/PC native pixel scale of $0\farcs0455$ pixel^{-1}, and registered to one another by fitting elliptical Gaussians to the galaxy core. The registration was done in this manner since, due to color gradients and the lack of UV emission from both the galaxy and globular clusters, the images do not lend themselves to good cross-correlation across many wave bands. We converted all images to flux density units (millijansky) using the STSDAS SYNPHOT package. We convolved all images to the resolution of the NICMOS F205W data by convolving them with circular Gaussians, following the method of Perlman et al. (2001). The resulting optical spectral index map is shown in Figure 4; note that we use the convention $S_\nu \propto \nu^{-\alpha}$.

2.2. VLA

We observed 3C 264 with the *VLA* in K band (22.5 GHz) and X band (8.5 GHz) in B configuration in June 2002, and in A configuration in August 2003 as part of program AP439. For these observations, 3C 286 was used as the primary flux density calibrator source, and the QSO J11503+24179 as the primary phase calibrator and secondary flux density calibrator. The same two sources were also used to determine the instrumental polarization parameters. The K-band observations were done using the VLA's fast-switching mode to calibrate out any phase fluctuations due to tropospheric variations. This entailed alternating between 125 s scans of 3C 264 and 45 s scans of the phase calibrator. The primary flux density calibrator was

observed with 70 s scans every hour. The X-band observations were used not only for imaging, but also as a pointing reference for the high-frequency observations. Two intermediate frequencies (IFs) were used in each band, each with a bandwidth of 50 MHz, and the average of the two was used to produce the final maps. In addition to our observations, we have also obtained C-band (5 GHz) A-array data from the online *VLA* archive (see Lara et al. 2004), in order to make a matched resolution 5 GHz–8 GHz spectral index map. For this data set also, 3C 286 and 3C 48 were used as the primary flux density calibrators, and the QSO J11503+24179 was used as the phase calibrator and secondary flux density calibrator.

The calibration of the C-band and X-band data sets was straightforward, following closely the recommended procedure in Chapter 4 of the AIPS Cookbook. Very little flagging was required for these data sets, and all of the antennas in the array were well behaved. Once calibrated, a clean map was made with several rounds of self-calibration, and deconvolution using the AIPS tasks CLEAN and CALIB. For the deconvolution, we used the "robust" or Briggs' weighting scheme to weight the visibilities and a restoring clean beam of $0\farcs482 \times 0\farcs365$ for the C-band data, one of $0\farcs246 \times 0\farcs218$ for the X-band A-array data, and one of $0\farcs76 \times 0\farcs68$ for the X-band B-array data. The rms noise level achieved in the C-band Stokes I image is 65 μJy beam^{-1}—on the order of the theoretical noise limit of 46 μJy beam^{-1}. The achieved noise levels in the X-band data were similarly close to the thermal noise limit. The other Stokes parameters were not solved for in these data sets, as the C-band polarization structure has already been published (see again Lara et al. 2004), and our X-band data lacks polarization calibrator observations.

The reduction of the K-band data was performed using mostly standard techniques in AIPS, following closely the recommended procedure given in Appendix D of the AIPS cookbook.[14] The first 10 s of every scan were flagged to account for mispointings at the start of scans. This was particularly important for this fast-switched data since the array elements have their pointings changed very frequently. Antenna 1 was flagged in all of the data due to very low amplitude measurements with respect to the rest of the array. This was in addition to any antennas that were flagged by the online data quality monitors. Also in both the A-array and B-array data, there was a tropospheric noise component, forcing us to flag the first and last hour of each data set.

After the initial flagging was done, we first solved only for the phase solutions of our primary phase calibrator, assuming a point source model. This allowed us to calibrate out any phase fluctuations induced by the troposphere. These solutions were found in 10 s intervals, and applied to only the phase calibrator and 3C 264. Amplitude and phase solutions were then found for both the primary flux density calibrator, 3C 286, as well as the secondary flux calibrator. For the former, a clean component model provided by AIPS was used, and for the latter, a point source model. The solutions for 3C 286 were used only to bootstrap the flux density scale for the other objects—phase solutions based on 3C 286 were not applied to other objects. Polarization calibration was performed using QSO J11503+24179 to solve for the polarization leakage terms (the "D-terms"), and using 3C 286 as the P.A. calibrator. Once the calibration was complete, clean maps were made as above, using several rounds of self-calibration and deconvolution with Briggs' weighting. A restoring clean beam of $0\farcs0844 \times 0\farcs0826$ was used for the A-array data and one of $0\farcs264 \times 0\farcs254$
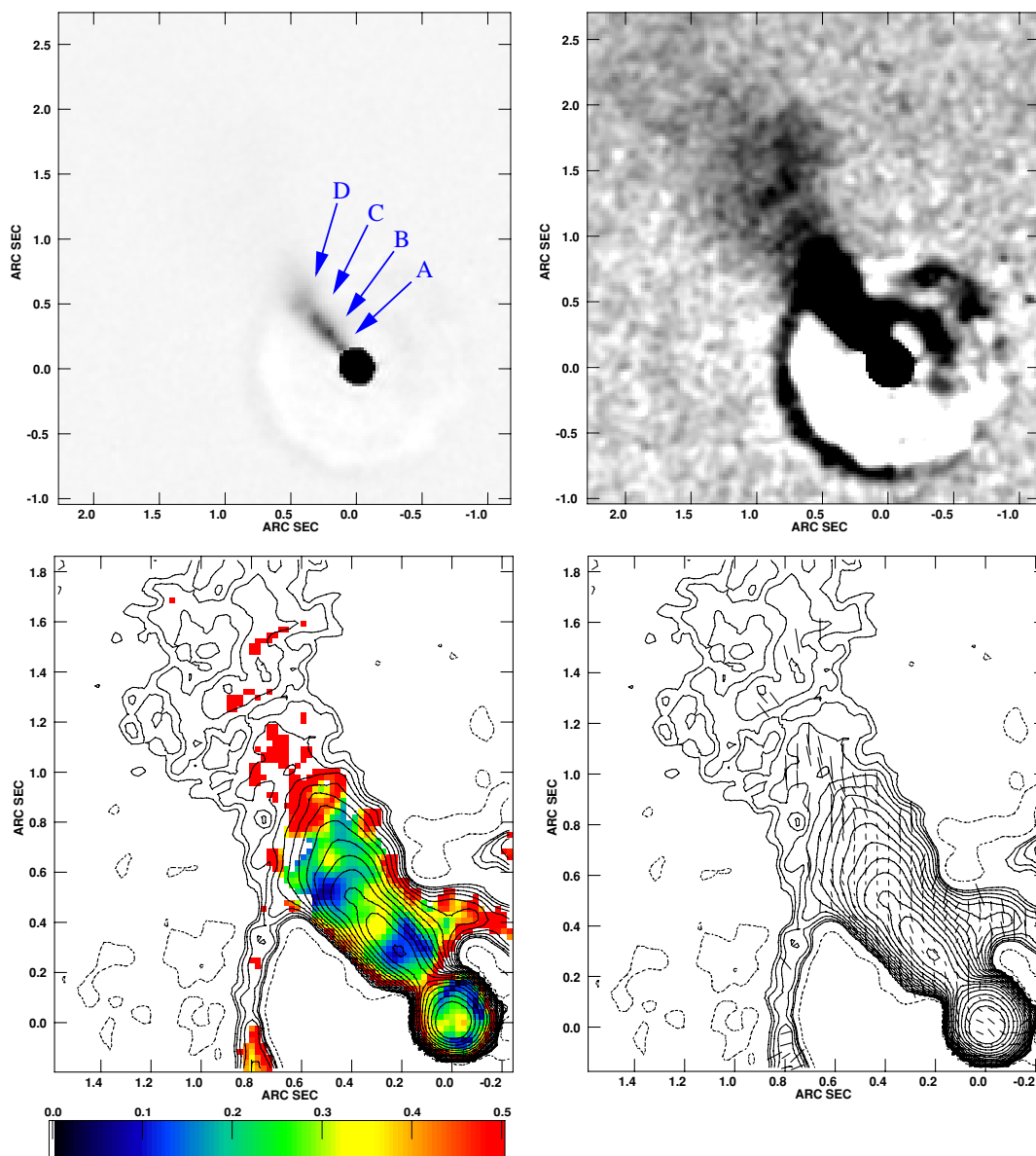
---

[14] See http://www.nrao.edu/aips/cook.html.

Figure 2. Optical (*HST* F555W) polarimetry of the 3C 264 jet (copied with permission from Perlman et al. 2006). The image scale is 440 pc arcsec^{-1}. Top left: Stokes *I* image scaled to bring out fine-scale structure within the knots. Top right: Stokes *I* image with stretch that saturates on bright regions, but helps bring out faint structure in this jet. In this view, the jet can be seen beyond the dust ring at 1″ from the nucleus (Sparks et al. 2000). Bottom left: fractional polarization (colors) overlaid with Stokes *I* contours—red indicates ≳45%. Bottom right: Stokes *I* contours with polarization (*B* field) vectors; a vector 0″.1 long represents 150% polarization; and contours are spaced by $\sqrt{2}$, with a base contour level of 1.783 counts s^{-1}.

for the B-array data. Again the rms noise limit achieved in each configuration was on the order of the theoretical noise limit—57 μJy beam^{-1} for the A-array Stokes *I* image and 68 μJy beam^{-1} for the B-array, compared to the theoretical limit of 42 μJy beam^{-1} for both configurations. For these data, we also mapped the Stokes *Q* and *U*, using the same "clean boxes" as were used to make the Stokes *I* image. From these the %P and P.A. maps were made, with the well-known Rician bias in P (Serkowski 1962) removed using the AIPS task polco. The resulting images are shown in Figure 3, and discussed in Section 3. Radio and radio–optical spectral index maps are shown in Figure 5.

2.3. Chandra Observations

We observed 3C 264 with the *Chandra X-ray Observatory* on January 24, 2004, using the ACIS-S instrument detector in faint mode with the object centered on the back-illuminated CCD, S3. This CCD was chosen due to its sensitivity in the soft X-ray regime. We used a 1/8 sub-array of the chip to mitigate photon pileup. A total of 38.3 ks was granted to this program, with 34.76 ks remaining after flagging out background flares.

The imaging data were processed using CIAO version 3.4.0, and CALDB version 3.2.2.[15] A new level 2 events file was created following the recommended procedure in the CIAO science threads, after which pixel randomization and the readout streak were removed. The sub-pixel event repositioning (SER) algorithm described by Li et al. (2004) was then applied to the event data, and an image was generated from the resulting SER-processed events by resampling at 0″.246, i.e., one-half of the native ACIS-S pixel scale. Following SER, we also applied a

---

[15] For a discussion of CIAO see http://cxc.harvard.edu/ciao.
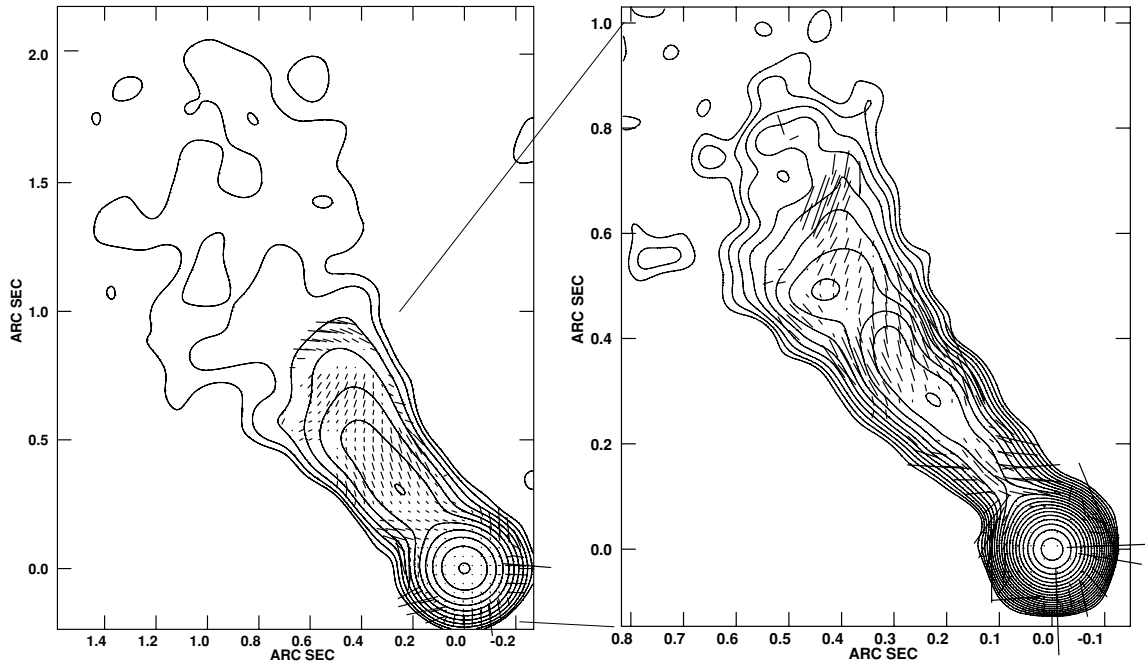
Figure 3. Fractional polarization maps made with VLA A-array data at 22.5 GHz. Contours represent Stokes *I*, and are spaced by powers of 2. Vectors are proportional to fractional polarization—0″1 corresponds to 100% polarized flux—and are rotated to represent projected magnetic field direction. Left panel: image made with a 800kλ taper applied. The base contour level is 0.138 mJy beam⁻¹. This taper reveals the faint part of the jet beyond 1″ from the core, which is also detected in the optical. Right panel: the same data, mapped without a UV taper. The base contour level is 0.171 mJy beam⁻¹. This full resolution map clearly shows the widening jet (Lara et al. 2004; see also Figure 4) as well as the dramatic drop in signal outside the "ring." Also note how the *B*-field vectors follow the flux contours until just before knot D, where they turn to the north–west, nearly perpendicular to the jet. This may be evidence of a weak shock.
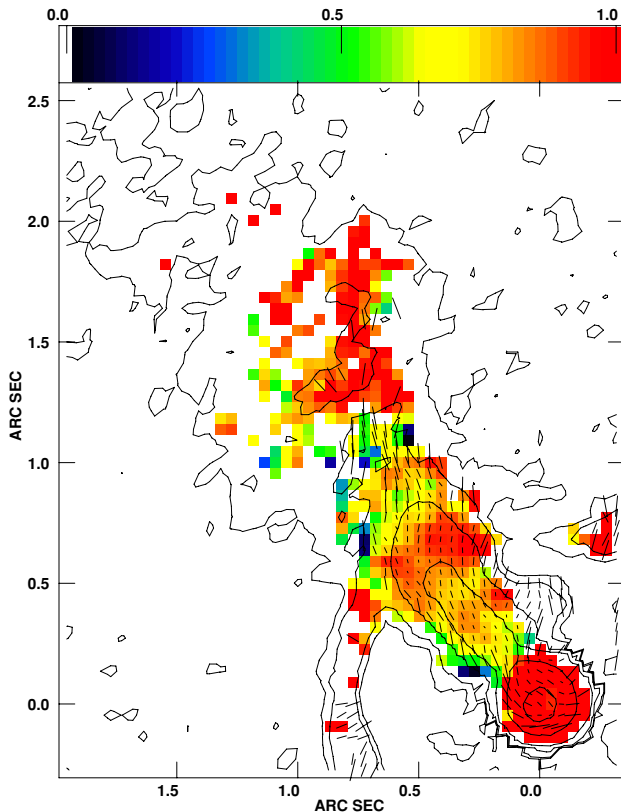

Figure 4. Optical fractional polarization map, obtained using the F555W WFPC2 data, overlaid on optical spectral index map. Base contour level is 6.6×10^{-4} counts s⁻¹ pixel⁻¹, in optical Stokes I, with contours spaced by factors of 4. Note that this image used the native PC pixel scale of 0″0455 pixel⁻¹, while Figure 2 was sub-sampled by 2. Vectors represent projected *B*-field direction, and their length is proportional to %P—a vector 0″1 long represents 150% polarization. The dust ring can be seen at approximately 0″8 from the core. Note the structure discussed in Sections 3.1 and 4.1.

maximum-likelihood deconvolution algorithm to the imaging data. This allowed us to maximize the angular resolution of the data and distinguish the jet from the core. The resulting image is shown in Figure 6 as contours, with the F555W image overplotted in color.

While CIAO version 3.4 is adequate for our imaging analysis, more recent available calibrations (CIAO version 4.1.2 and CALDB version 4.1.3) were used to make a new level 2 events file and construct calibration data for spectral fitting. A spectrum of the X-ray source core was extracted from the events file using a circular aperture with a radius of 1″23 (five post-SER pixels) and a local background region, via the CIAO script PSEXTRACT. For active galactic nucleus (AGN), this region typically contains 95% of the core flux (Marshall et al. 2005), and so no aperture correction was applied. The instrument response matrix and ancillary responses were generated using the CIAO tasks MKACISRMF and MKARF. We discuss in Sections 3.3 and 4 the X-ray and broadband spectrum of the jet and its physical implications.

3. RESULTS

In this section, we present the results of the above analysis, and compare them to previous work. We start with general morphological descriptions of the 3C 264 jet in all analyzed wave bands, as well as the broadband spectral characteristics. Then, we discuss the *HST* optical and VLA radio polarimetric properties of this source, as well as its X-ray morphology and spectrum.

3.1. Radio–Optical Morphology and Spectrum

3C 264 has a Fanaroff–Riley type I radio structure (e.g., Fanaroff & Riley 1974) with a head–tail morphology and bent
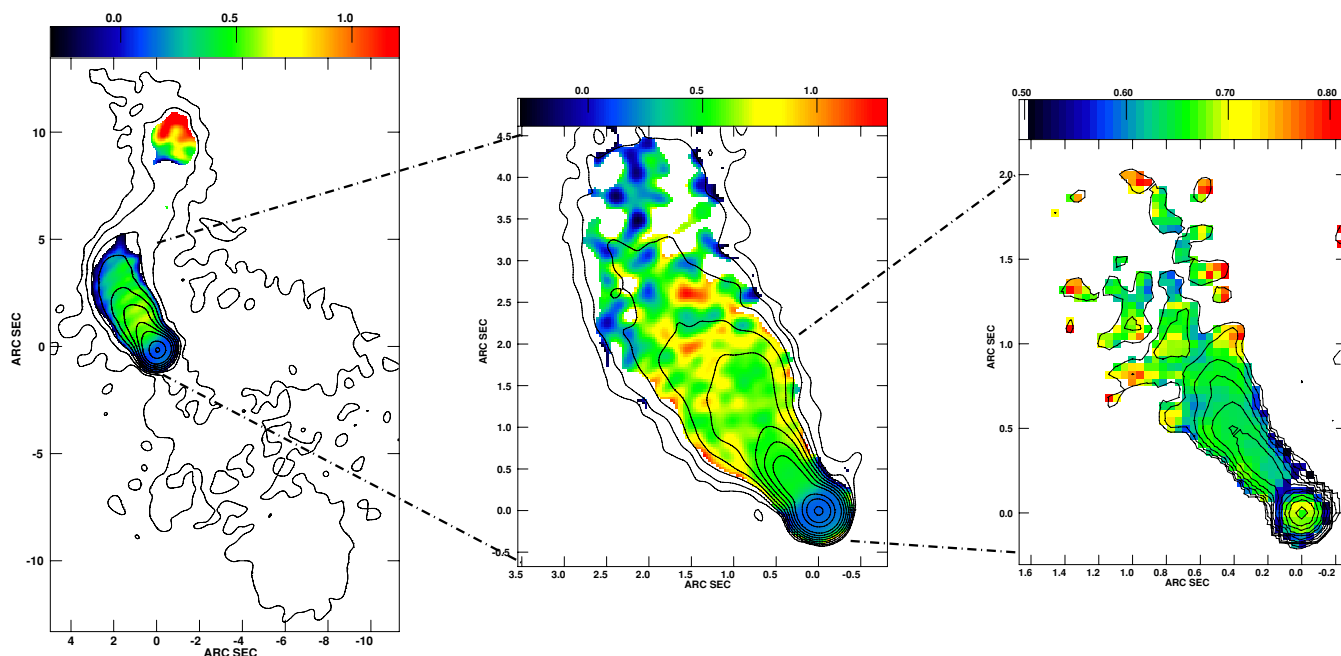
Figure 5. Radio and radio–optical spectral index maps. In all plots, the contours are spaced by powers of 2 and the color table is as given. Left: spectral index map between 5.0 GHz and 8.5 GHz, at $0\rlap{.}''5$ resolution. Base contour level is 0.203 mJy beam^{-1}. Middle: spectral index map between 8.5 GHz and 22.5 GHz, at $0\rlap{.}''3$ resolution. Base contour level is 0.835 mJy beam^{-1}. Right: spectral index map between 22.5 GHz and F555W *HST* data, at $0\rlap{.}''2$ resolution. Base contour level is 0.013 mJy pixel^{-1}. Note the relative constancy of the spectral indices in the inner $1''$ of the jet.

jet. As can be seen in our radio maps (Figure 5), the radio jet extends $\sim 25''$ along a direction that is initially northeast, but bends through $\sim 90°$ to the west at $3''$–$6''$ from the nucleus, and then back toward the northeast at greater distances (Gavazzi et al. 1981; Bridle & Vallee 1981; Baum et al. 1998; Lara et al. 1999). On these size scales, the jet is seen only in the radio. Our 8.5 GHz, B-array map (left panel of Figure 5) shows a morphology similar to that described in Lara et al. (1997, 2004) at lower frequencies. All these images show a relatively smooth morphology between $2''$ and $4''$ from the core, a region where the jet begins a bend through about $90°$. By a distance of $4''$ from the core, the jet has reached a nearly north–south orientation, and then becomes northwesterly for several arcseconds before bending back to the northeast at about $10''$ from the core at the location of a fairly significant knot. Radio structure on larger scales (after this second bend) has been discussed by Lara et al. (1997, 2004).

Along with the radio maps, Figure 5 also shows the radio spectral indices. The left-hand panel shows the radio spectral index between 5 and 8.4 GHz. As can be seen, the spectral index $\alpha_5^{8.4}$ is ~ 0.5 throughout the jet's first $\sim 4''$, out to the location of the first bend. The structure at the locus of the second bend is somewhat steeper spectrum, particularly at its downstream end. The middle panel of Figure 5 shows the spectral index of the jet between 8.4 and 22.5 GHz. As can be seen, we see a spectral index of $\alpha_{8.4}^{22} \sim 0.5$ throughout the entire jet out to $\sim 2''$ from the core, with somewhat flatter spectral indices at greater distances, where the bend begins. From the C–X spectral index map, we find the radio spectral index of the core of 3C 264 to be $\alpha_{\rm core} \simeq 0.14$, consistent with previous results (cf. Lara et al. 2004). The radio spectral index of the inner jet is also consistent with previous results, around $\alpha \sim 0.5$.

The optical morphology of the inner $1''$ of the 3C 264 jet (Figure 2) is similar to that seen in the 22.5 GHz A-array map
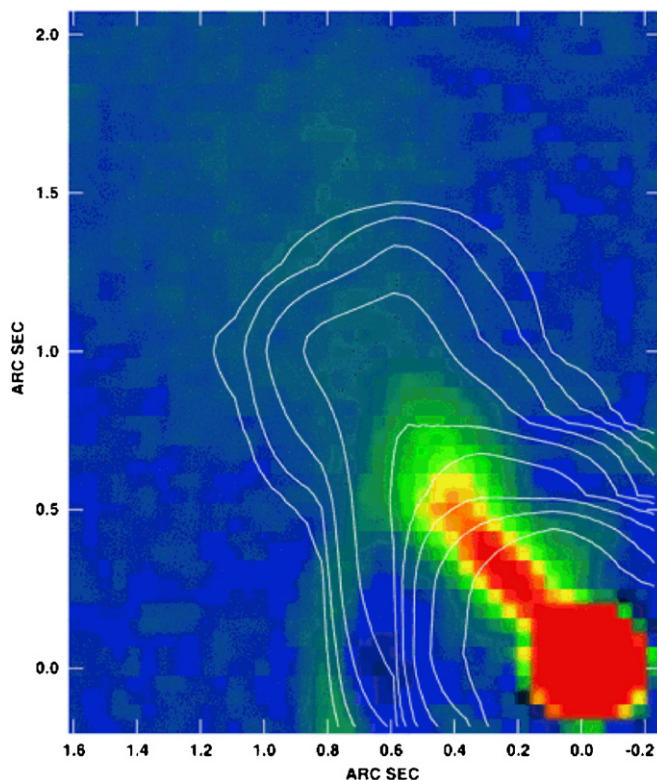

Figure 6. *Chandra* X-ray image of 3C 264 (contours), plotted over the F555W Stokes I image (color). The *Chandra* data have been processed according to the procedure in Section 2.3, deconvolved using a maximum entropy algorithm, interpolated onto the PC pixel scale, and then smoothed with a 1-pixel Gaussian. X-ray contours are spaced by factors of 2, with a base level of 5.725×10^{-2} counts pixel^{-1}. Note that X-ray emission is detected from at least two distinct regions in the jet.
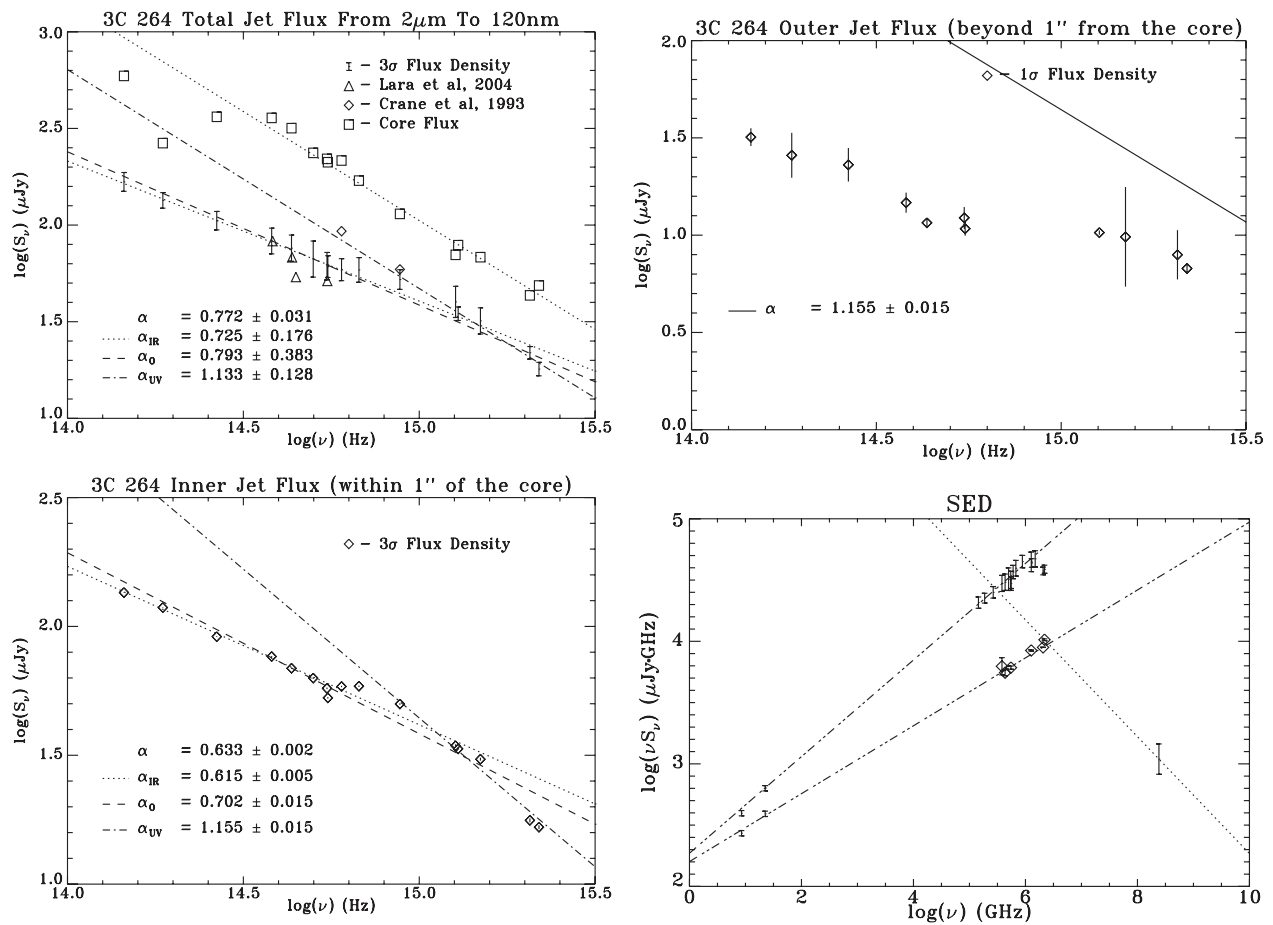
Figure 7. Optical spectrum and spectral energy distribution of the 3C 264 jet. Top left panel: total jet flux and spectrum in the optical. For the jet, we show fluxes from three studies here: our own (error ranges), Lara et al. (2004), and Crane et al. (1993). We also show fluxes for the core as taken from our data. For the total jet flux, note the excellent overlap of our points with those from Lara et al. (2004). The flux points of Crane et al. (1993) are, however, clearly seen to be discrepant, particularly in the red. See Section 3.1 for details. Bottom left panel: inner jet flux and spectrum in the optical. This plot shows fluxes from our *HST* data for the region of the jet within 1″ of the core. Lines are shown describing the spectral indices in the radio–optical, IR, optical, and ultraviolet. Top right panel: outer jet flux and spectrum in the optical. This plot shows fluxes from our *HST* data for the region of the jet at distances greater than 1″ from the core. Bottom right panel: spectral energy distributions of the inner jet (upper values) and outer jet (lower values). The dash-dotted lines represent a simple power-law fit to the radio and optical data for both the inner and outer jets, and the dotted line represents the same fit to the UV to X-ray data for the outer jet. For the inner jet, optical data with frequency above $10^{14.5}$ Hz were not included. For the outer jet, all optical data were included. Lines are shown describing the spectral fits. See Section 3.1 for details.

(Figure 3). Both maps show a jet that has a surface brightness, which varies smoothly along the ridgeline. A few faint knots appear, and we have termed them A–D in order of increasing distance from the nucleus (pointed out in Figure 2). The jet fades precipitously outside of ∼1″ from the core (this last section is not seen well in the UV image), where a prominent dusty disk or "ring" is located. While this might suggest an interaction between the disk and the jet, the jet viewing angle has been found to be ∼50° (Baum et al. 1997; Lara et al. 1997). The disk is more likely viewed face-on, however, due to its nearly circular shape and apparent lack of rotation (Baum et al. 1990, 1992). Thus the likelihood of interaction is small, although not out of the question (see Baum et al. 1997 for a discussion). Outside of this "disk," the F555W Stokes *I* image shows jet emission continuing out to roughly 2″–2″.5 from the core, emission that is also seen in both our 22.5 and 8.4 GHz data (Figure 3 and also middle panel of Figure 5) as well as the MERLIN 1.5 GHz map of Lara et al. (2004).

We also produced a map of the radio–optical spectral index, shown in the right-hand panel of Figure 5. This varies between $\alpha_{RO} = 0.6$–0.7 over the vast majority of the inner jet (i.e., within 1″ of the core). The radio–optical spectral indices seen along the jet centerline are slightly flatter (i.e., harder) than those

seen along the jet edges (throughout the optically seen portion of the jet), as well as possibly along the jet's northern edge at distances <0″.5 from the nucleus. The $\alpha_{8.4}^{22}$ map also shows steeper spectral indices along the jet edges than in the center, beginning at distances of ∼0″.5 from the nucleus, as well as the slight flattening of the spectrum at the jet's northern edge within the first 0″.5. Thus, contrary to some other jets (e.g., M87; Perlman et al. 2001), the first 2″ of the 3C 264 jet (i.e., the portion seen in the optical) shows a remarkable consistency in its radio–optical spectral energy distribution (SED).

The *HST* data show that the morphology of the jet is smooth and consistent from the IR to the UV, at least at the 0″.1 level. This is reflected in the smooth variations seen in the optical spectral index map of Figure 4. But at the smallest scales we can resolve (as seen on both *HST* UV images as well as the full-resolution F555W Stokes *I* image), the knot-like surface brightness enhancements A–D become pronounced, indicating that the overall smoothness may be simply a resolution issue. This is supported by the more knot-like structure seen in the 1.6 GHz MERLIN maps of Lara et al (2004).

In Figure 7, we plot the optical spectrum and SED for the jet and core, as seen in our data. The optical spectral index for the entire jet (all pixels > 3σ), is found to be $\alpha_O = 0.77 \pm 0.03$.

This is harder than that of the core, in contrast to previous results around $\alpha_O \sim 1.4$ of Crane et al. (1993) and Lara et al. (2004). These latter points are also plotted in the top left-hand panel of Figure 7. As can be seen, the fluxes for the two previous studies are not consistent with one another: at a similar frequency, Crane et al. (1993) found a flux nearly a factor 2 higher than did Lara et al. (2004). However, Crane et al. did not model the galaxy, instead using 20-pixel-wide strips located above and below the jet to subtract out galaxy emission. The likely result of their procedure is to undersubtract the galaxy, particularly in the red and indeed, we can see that their F342W point falls within the error bars of (although slightly above) our F330W flux, while their F502W flux point is nearly a factor 2 higher. This corroborates our assertion that their spectral index estimate was contaminated by incorrect subtraction of galaxy light. For the Lara et al. (2004) points, the issue is more subtle, as we see fluxes very consistent with the ones we report. However, as shown in Figure 6, Lara et al.'s (2004) data spanned only ~0.2 decades in frequency, giving a small pivot in their spectral index fits. Our data span more than a decade in frequency, which removes ambiguity in the fit. In the same figure, we show lines for best-fit spectral indices in the infrared, optical and UV bands. As expected, the errors on those fits are far larger than when all the *HST* data are used (by factors of 4–14); this illustrates the danger in using a spectral index based on data spanning only a small fraction of a decade in frequency. Our data show no evidence of a change in spectral index from the infrared to the optical; however, there is possible evidence (2.3σ) for a steepening of the spectral index to the ultraviolet. The same plot shows the spectrum of the core in the optical. As can be seen, the spectral index of the core throughout the infrared to UV is remarkably similar to that for the jet (although the core is more than a factor 2 brighter), although the core shows no evidence for hardening toward the ultraviolet. This strongly suggests that the same emission mechanism dominates the emissions of the two, although other data also show a jet spectrum that is noticeably harder than that of the core in the blue (Hutchings et al. 1998).

Figure 6 (bottom left panel) shows the fluxes for the inner jet (within $1''$ of the nucleus) along with spectral index fits for the entire *HST* band, infrared, optical, and ultraviolet. As can be seen, the spectrum of the inner arcsecond of the 3C 264 jet is somewhat flatter than that of the entire jet, with an average spectral index $\alpha = 0.633 \pm 0.002$. The spectrum of the inner jet is slightly but significantly steeper (0.702 ± 0.015 compared to 0.615 ± 0.005) in the optical than it is in the near-infrared, with a more significant steepening in the ultraviolet ($\alpha_{UV} = 1.155 \pm 0015$). These values are, it should be noted, within 1σ of the values seen for the jet as a whole, as is sensible, since the errors should be largest in the outer jet, where the jet is faintest. Those pixels therefore dominate the larger errors in the previous spectral index fits. Figure 6 (top right panel) shows the spectrum of the outer jet (at distances greater than $1''$ from the core). As expected, the errors are much larger for this region.

Figure 4 shows a detailed spectral index map for the optical regime, overplotted on the F555W polarimetry. This map shows significantly more structure than that seen in the α_{RO} map (Figure 5), indicating that the SEDs of some parts of the jet are turning over in the optical. The most significant feature of the optical spectral index map is a softening by $\Delta\alpha_o \approx 0.2$ in a $0''2$ long region, nearly coincident with the location of the dust ring. This softening may be a result of galaxy subtraction residuals, or it could be indicative of increased energy losses. The latter would

suggest an interaction between the jet and the ring (as mentioned above). However, it is hard to comment on this definitively since the galaxy had to be modeled independently in each *HST* image as its inner $1''$ changed significantly from the IR to the UV. Outside of the ring, the optical spectral index is generally steeper than that seen in the inner jet, a feature that was also seen in the α_{RO} map. Some interesting structure is also seen interior to the ring, where along the jet ridgeline we see flatter optical spectral near the loci of the knots, with steeper values of α_O both along the jet's edges as well as in the region between knots B and C. We find the core's optical spectral index to be $\alpha \simeq 0.9$, which, when the radio core spectral index is taken into account, indicates a spectral break of $\Delta\alpha \sim 1$ in the core spectrum around 10^{13} Hz.

3.2. Multi-band Polarization

The optical polarization characteristics of the 3C 264 jet have been discussed already (using the same WFPC2 data) by Perlman et al. (2006). However, it is useful to reprise the discussion here in view of the new VLA and ACS polarization data. We see an average fractional polarization level of ~20% along the jet, roughly similar to that seen in the radio, and projected magnetic field vectors that generally follow the flux contours. As noted there, in our WFPC2 F555W data (Figure 2) we find a polarization morphology that is quite homogeneous, in line with the overall smooth appearance of the jet. Coincident with the flux maximum of knot B (see the bottom left panel of Figure 2), there is a significant minimum in optical polarization of $\simeq 10\%$ (see Figure 8). No change is seen, however, in the optical magnetic field vector direction at this location. Just downstream of this, the optical polarization increases to $\simeq 35\%$. A second decrease in optical polarization is seen to coincide with the upstream edge of the dust ring, along the jet's ridgeline. Also beginning at about $0''5$ from the core, the optical magnetic field vectors are seen to rotate by about $30°$ to assume more of a north–south orientation, particularly along the northern edge of the jet. In the optical, at the jet edges the level of polarization increases to upward of ~50%, and the projected *B*-field tends to be less aligned with the jet direction.

The F330W ACS HRC polarization data (Figure 9), while much lower signal to noise (thanks to the shorter exposure time), sheds light on some regions of the inner jet of 3C 264, thanks to its higher resolution. In particular, we see that the knots in the inner jet do, in fact, have significant polarization P.A. changes in the optical. In particular, in knot A, we see a low polarization region toward the western side of the knot maximum, continuing through the ridgeline and then winding around to the eastern side of the knot B maximum. Where we do see significant polarization in knot A, on the eastern side, it has an orientation ~90° from the jet direction. Patterns of this type have been seen in other jets, such as in the knot C region of the jet of 3C 15 (Dulwich et al. 2007). Knot B's maximum is seen to have a north–south magnetic field configuration, which persists into the B/C interknot region. Finally, in knot D, we see a zero-polarization region along the ridgeline, with a higher polarization region downstream where the magnetic field vectors become perpendicular to the jet direction in the jet center, and parallel to the jet direction along the eastern and western edges of the component. This pattern is similar to that seen in some features in the M87 jet, in particular its knot D (Perlman et al. 1999). We will comment on these issues in greater detail, along with their physical implications, in Section 4.
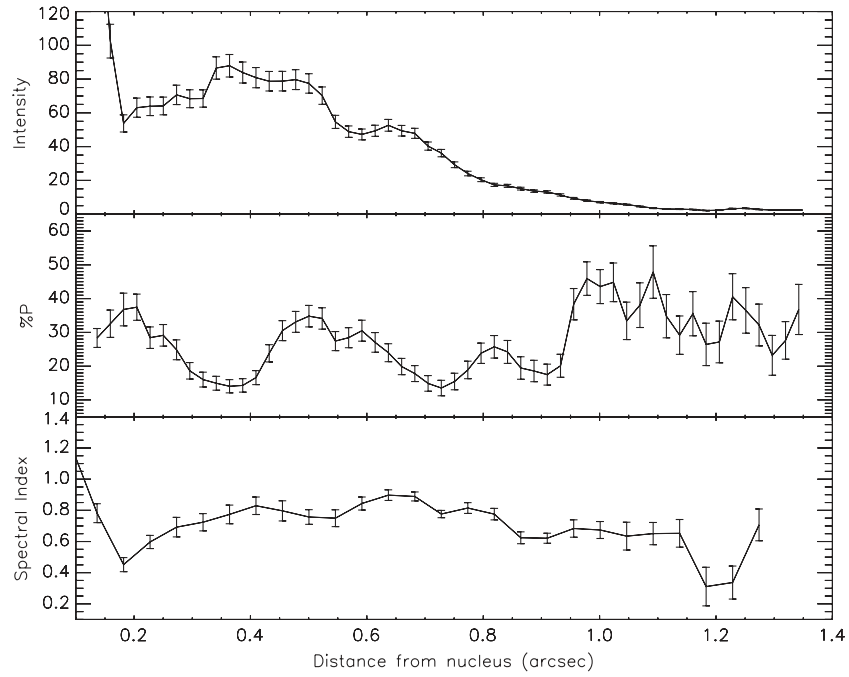
Figure 8. Cross sections along jet of (top panel) intensity, (middle panel) %P, and (bottom panel) optical spectral index. Note the clear polarization minimum at the jet intensity maximum between 0″.3 and 0″.4 from the core.
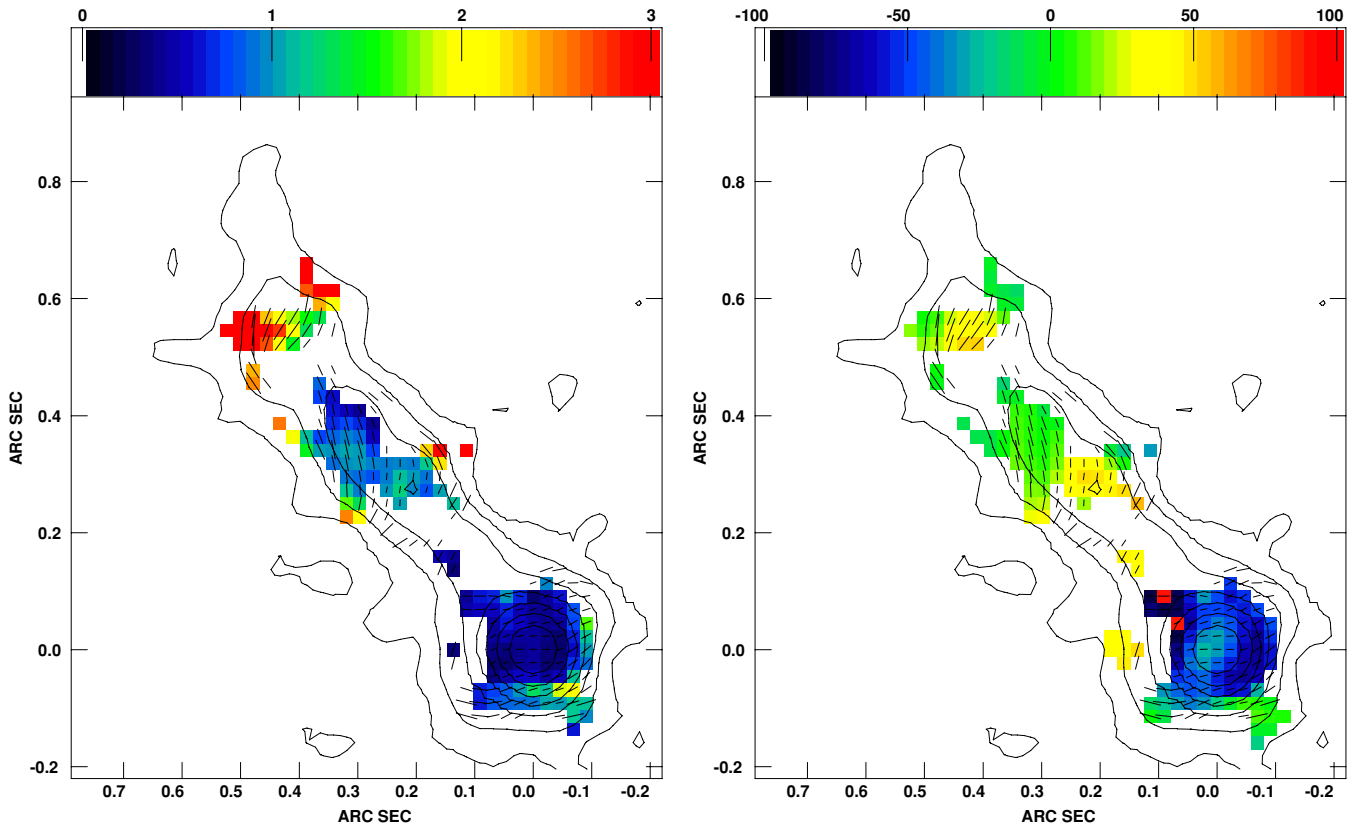

Figure 9. High-resolution ACS F330W polarization data. At left, the color scale shows the ratio of F330W polarization to that seen in F555W at lower resolution, while at right, we show in color the difference in position angle. In both panels, we show contours in F330W flux along with polarization vectors taken from those data. Flux contours are plotted at 4.571×10^{-2} counts s$^{-1} \times$ (1, 2, 3, 4, 6, 8, 12, 16, 24, 32, 48, 64, 128, 192, 256, 512, 1024). The vectors represent *B*-field direction, and a vector 0″.1 long represents 100% polarization. Note that the F330W data has a resolution more than a factor of 2 better than the F555W data, thanks to its shorter wavelength and smaller pixel size. Thus despite its significantly lower S/N (a product of its much shorter exposure time), it reveals the highest resolution detail in the polarization structure of the optical/UV emitting part of the 3C 264 jet. All of the differences seen in this image as compared to Figure 4 can be attributed to the higher resolution. See Section 3.2 for details.
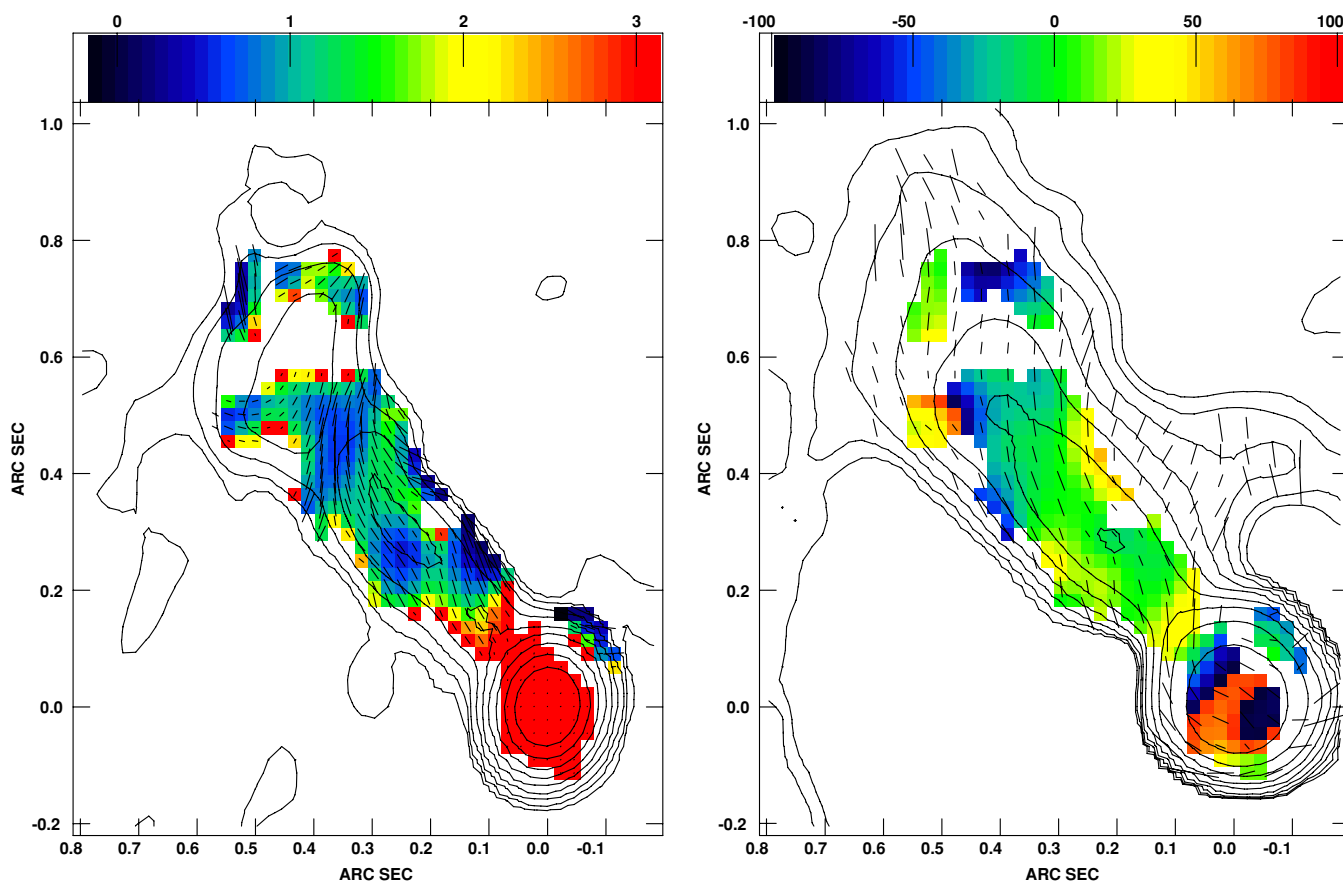
Figure 10. Comparison between optical and radio polarization in the 3C 264 jet. At left, we show the 22.5 GHz, A-array polarization map of Lara et al. (2004; contours and polarization vectors) overplotted onto a color image showing the ratio of optical to radio polarization, while at right, we show the F555W polarization data (contours and polarization vectors, but with vectors shown only every other pixel) overplotted onto a color image showing the difference in polarization P.A. between the optical and radio data. In the left panel, contours are plotted at $4.522 \times 10^{-3} \times (1, 2, 4, 8, 16, 32, 64, 128, 256, 512, 1024)$ Jy beam^{-1}, whereas in the right panel, contours are plotted at $2.529 \times (1, 2, 4, 8, 16, 32, 64, 128, 256, 512, 1024)$ counts s^{-1}. As can be seen, there are several regions where significant differences are seen between the degree of fractional polarization seen in the optical and radio, but the differences in polarization position angle are small (note that the one region where there appear to be some differences is very close to 180° and hence degenerate.

Many similar features are seen in the *K*-band radio polarimetry data (Figure 3), however some differences also appear. In Figure 10, we summarize the differences and similarities in polarization properties between the optical and radio polarization data. We see broad similarities in several regions of the jet. In particular, the radio data show a similar level of fractional polarization, when averaged along the jet, as well as the same general trend in the orientation of the magnetic field vectors. We also see a similar increase in the fractional polarization toward the jet edges, as well as a change in the orientation in the magnetic field vectors toward a more northern direction. This latter trend at first blush appears to be correlated with some differences in the ΔP.A. map shown in the right panel of Figure 10; however, one must recall the 180° degeneracy that is inherent in polarization data, and indeed closer inspection of both data sets reveal that this is the nature of the red "band" apparent in that panel at this location. This region is, however, seen to have a somewhat lower polarization in the optical than in the radio.

Upon closer inspection of Figure 10, however, we see several more significant differences between the optical and radio polarimetry. In particular, near the maximum of knot B, where a minimum was seen in the F555W polarization data, we see that the radio data do not show a similar feature (see Figure 10, left panel). Instead, we see in the radio map just upstream of that region (coinciding with knot A and upstream), a decrease in the radio polarization, to a value of only ∼5%, in a band

that extends across the entire jet. A closer look at the F330W data, however, does reveal a somewhat similar feature in this region, but it is still considerably narrower in the optical, where it is seen to stretch east–west across the jet from west of knot A to east of knot B. The knot A–B region exhibits similar orientations of the polarization vectors in the optical and radio. Even stronger differences are apparent in a region 0″.7–0″.8 from the nucleus that extends across nearly the entire jet width. In this region, which corresponds to the peak of knot D, no significant polarization is detected in the *K*-band data, while in our F555W data the polarization is also somewhat decreased, but higher, between 10% and 15%. This region, the downstream end of which coincides roughly with the location of the dust ring's upstream edge, also marks the location of a subtle change in the orientation of the optical magnetic field vectors to a north–south orientation. A look at the higher resolution, but lower signal-to-noise F330W data does reveal a low optical polarization region right at the peak of knot D, and downstream magnetic field vectors that seem to surround the component, running parallel to the local flux contours, including perpendicular to the jet direction at the ridgeline. The low optical polarization region is seen in the F555W data to continue out to the far edge of the dust ring. This could be a result of scattering due to the dust in the ring. These features will be discussed in more detail in Section 4.

On larger angular scales (e.g., beyond the dust ring), the optical surface brightness of the jet decreases precipitously.
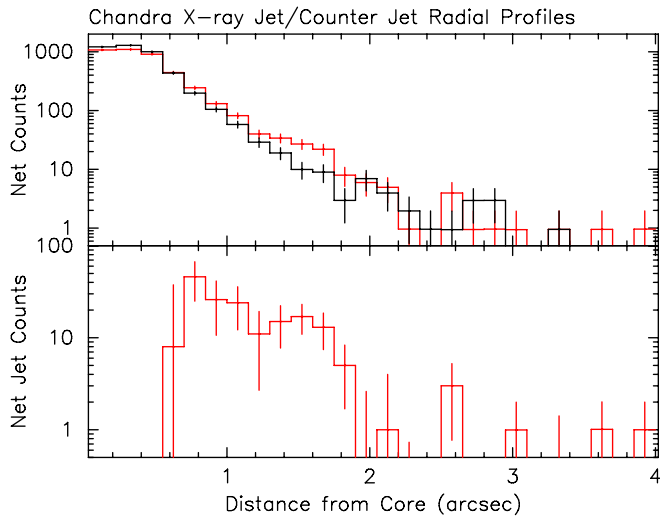
Figure 11. Top panel: *Chandra* X-ray count profiles along jet (red) and counter jet (black). Bottom panel: counter-jet profile subtracted from jet profile. Note the significant excess between ∼0″.8 and ∼1″.8.

(A color version of this figure is available in the online journal.)

Nevertheless, we detect significant optical polarization in this regions, with $P = 30\%$–40% in a large region near the northern edge of the jet, extending between distances ∼0″.9 and 1″.5 from the core. In this region, the magnetic field vectors appear to be aligned approximately with the jet, although the error bars and scatter on them are large. The same region shows a similar radio polarization (see Figure 5 of Lara et al. 2004), and P.A. (note that Lara et al. plot *E* vectors rather than implied *B*, as we do). We do not have the signal to noise to follow the polarization of the jet beyond this point, in the region where the jet is seen to bend through 90°, where the 5 GHz map of Lara et al. shows an east–west magnetic field vector and a somewhat smaller polarization.

3.3. X-ray results

Our deep *Chandra* observations (Figure 5) reveal X-ray emission from one and perhaps two regions of the jet, as well as the AGN itself. One of those two regions lies well beyond the optically bright part of the jet (at >1″.5 from the core), while the other is on scales less than 1″, and thus very close to the size of the *Chandra* High Resolution Mirror Assembly (HRMA) PSF. Therefore, it was necessary to be very careful with our treatment of the *Chandra* observations. This entailed not only the use of SER and deconvolution techniques (described in Section 2.3), but also exacting statistical tests.

We first generated a simulated PSF with ChaRT (Carter et al. 2003) using the total spectrum extracted from the source (see below) as input for the ray-tracer, as well as the source position found from centroiding. We characterized the PSF asymmetry in the X-ray image along the optical jet axis (∼40° east of north), by extracting source counts from the simulated PSF in symmetric regions on both the jet and counter-jet sides of the core. The asymmetry in the PSF favors the counter-jet direction and was found to be approximately 30%. We use the asymmetry estimate as a systematic error term when calculating the net jet counts, which we added in quadrature to the propagated statistical errors. Next, we extracted background subtracted radial profiles spaced by ∼0″.15 in the jet and counter-jet directions from the sub-sampled SER event file. Before extracting these profiles, we excluded all events outside of a 1″ wide strip along the jet direction.
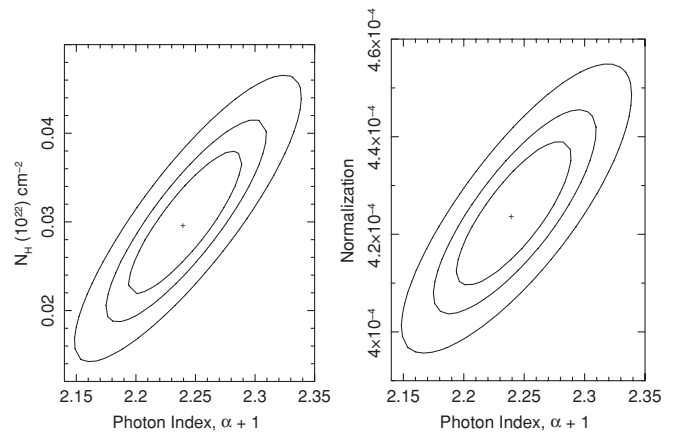

Figure 12. Parameter uncertainty contours for the X-ray spectrum of the core fitted to an absorbed power law. Left panel: spectral index against N_H. Right panel: spectral index again normalization in units of cm^{-2} s^{-1} keV^{-1}. χ^2 contours are 1σ, 90%, and 99% for two interesting parameters. See Section 3.3 for details.

By directly comparing the jet to counter-jet profiles, we were able to detect a significant excess of counts on the jet side in the *Chandra* image, between 0″.7 and 1″.8 from the core. This excess is shown in Figure 11. The jet component appears to have an approximately flat (within the errors) surface brightness profile at these radii. Thus, while the jet is clearly resolved in the X-rays, it is not possible with these data to comment in any more detail on the structure of the X-ray emission between 0″.7 and 1″.8 from the nucleus of 3C 264. Note that while jet emission is likely detected as close as 0″.5 from the AGN, it is much harder to quantify the jet emission inside of 0″.7 due to the presence of the much brighter nucleus. This latter region, unfortunately, coincides with the innermost of the two regions that the eye picks out in Figure 6.

The 0.3–10 keV X-ray spectrum of the core, containing 10,584 net counts and binned to a minimum of 30 counts per channel, is found to be well fitted by an absorbed power law with $\alpha = 1.24 \pm 0.05$ (1σ error bars for two interesting parameters; $\chi^2_{min} = 138$ for 152 degrees of freedom). As shown in Figure 12, the absorption is consistent with the Galactic value of $N_H = 2.45 \times 10^{20}$ cm^{-2} (from the COLDEN program provided by the *Chandra* X-ray Center, using data from Dickey & Lockman 1990). The intrinsic luminosity over the energy band 0.5–8 keV is 1.6×10^{42} erg s^{-1}. Results are in agreement with Donato et al. (2004: *XMM-Newton*) and Evans et al. (2006: *Chandra*) when the same energy bands are compared.

While the core is so bright that the choice of background region on the chip makes little difference to its fitted X-ray spectrum, much of this "background" is from the cluster A1367, within which 3C 264 resides. There is also evidence for thermal emission on a smaller spatial scale associated with the gaseous atmosphere of NGC 3862, the host galaxy of 3C 264. This was first noted by Donato et al. (2004) using *XMM-Newton* data, but a measurement of the gas properties was limited by the larger PSF of *XMM-Newton* and the fact that the source was far from the optical axis of the telescope. The first *Chandra*-based study of A1367 was done by Sun et al. (2005); however, that work did not discuss 3C 264 in depth as it was carried out with an earlier data set centered on the cluster center, which is 8′ distant from 3C 264. Sun et al. (2007), using the same *Chandra* data set observations as herein, measured an excess of soft X-ray counts compared with the PSF in an annulus of radii 1″.5 and 6″ (0.7–2.6 kpc) centered on the nucleus of 3C 264. They

found $kT = 0.65^{+0.29}_{-0.09}$ keV for this emission. We find some evidence for the presence of gas even in our core spectrum, with χ^2 decreasing by 11 if such a component is included. The temperature is cooler than found by Sun et al. (2007), at $kT = 0.30^{+0.11}_{-0.06}$ keV, indicative of complex thermal structure in the galaxy. The inclusion of the thermal component does not significantly affect the spectral index of the dominant power-law emission, however (with a thermal component we obtain $\alpha = 1.18 \pm 0.04$). Its normalization is reduced by about 5%, but since this is roughly the same as the percentage of missing flux due to the wings of the PSF, the normalization in Figure 12 is a good representation of the 1 keV flux density of the nucleus ($0.28 \pm 0.01 \mu$Jy).

Following the method described in Section 2.3, the net count rate in the resolved jet is $(4.5 \pm 1.1) \times 10^{-3}$ count s^{-1}. Adopting the spectral index of the core gives a 1 keV conversion factor of 1028 nJy count^{-1} s (0.5–8 keV), similar to the canonical value of 1000 nJy count^{-1} s of Marshall et al. (2005), and thus a 1 keV flux density for the resolved jet of 4.6 ± 1.1 nJy. This flux only applies to the jet outside of $0\farcs8$ from the core, for the reasons discussed above. We should also note that if the jet does in fact extend into the core, as the optical and radio jets do, then the core spectrum discussed above will be contaminated by jet components. Assuming that the X-ray flux beyond $1''$ is indeed due to the jet, we find an optical to X-ray spectral index for the outer jet of $\alpha_{\rm OX} = 1.48 \pm 0.06$. Combining this with our fitted radio-to-optical spectral index for the outer jet of $\alpha_{\rm RO} = 0.723 \pm 0.003$, we can estimate the minimum spectral break frequency and the minimum break in α. Doing so, we find (again, for the jet outside of $0\farcs7$) $\nu_{\rm break} \gtrsim 2 \times 10^{15}$ Hz, and $\Delta\alpha \gtrsim 0.85$.

4. DISCUSSION

In the preceding sections, we have discussed in detail optical and radio polarization images of the jet of 3C 264, as well as its optical and broadband spectrum and the results of a deep *Chandra* X-ray observation. As already discussed, this jet displays a smooth morphology in both optical and radio. The differences we see in polarization morphology, while less drastic than those seen in, e.g., M87 (Perlman et al. 1999), are nevertheless significant. We also find significant variations in the optical and radio–optical spectrum of the jet. X-ray emission is also seen from the jet on scales between $0\farcs7$ and $1\farcs8$ from the nucleus. In this section, we discuss the inter-relationship of these properties and their relevance to the overall physics of the 3C 264 jet. We will also discuss other jets where radio and optical polarimetry has recently been done, in particular M87 (Perlman et al. 1999, 2001; Perlman & Wilson 2005), 3C 15 (Dulwich et al. 2007), and 3C 346 (Worrall & Birkinshaw 2005; Dulwich et al. 2009), and their relationship to this source.

4.1. The Physics of the 3C 264 System

3C 264 is a highly interesting radio galaxy that contains many elements that are important to understanding both the AGN phenomenon as well as jet physics. The data discussed herein allow us to place significant new constraints on the physics of the nucleus and jet, and also to comment on the nature of the host galaxy environment. The latter is quite interesting in and of itself, as the host galaxy to 3C 264, namely NGC 3862, lies within—but not at the center of—a rich cluster that has complex substructure. Cortese et al. (2004) have found that Abell 1367, the surrounding cluster, lies at the intersection of two filaments

within the Great Wall, and is likely in the midst of its formation process. The cluster has a large number of subclumps and grouping, as revealed by multi-object spectroscopy and X-ray studies (Cortese et al. 2004; Sun et al. 2005, 2007). NGC 3862 itself lies at the center of a compact group within the cluster that consists of 18 galaxies (Lipovka et al. 2005). Our *Chandra* X-ray data reveal that the complicated temperature structure of the A1367 system continues down to scales of kpc, with evidence of a cooling-flow like structure within the subgroup.

NGC 3862 was dubbed "optically dull" by Elvis et al. (1981), referring to the relative strength of nuclear X-ray to optical emission. Further investigation of galaxies with similar characteristics (sometimes called X-ray bright optically normal galaxies, or XBONGs) have normally found that they can be fitted into the scheme of conventional accretion models if there is a moderate amount of nuclear gas ($N_{\rm H} \sim 10^{21}$ cm^{-2}) and dust ($E(B - V) \sim 0.5$–0.8) covering large solid angles (e.g., Civano et al. 2007). While our *HST* images do show a dusty disk a few hundred parsecs from the AGN, this disk does not appear to continue all the way to the center, and indeed, we find no evidence of reddening or absorption of the nucleus, based both on our *HST* and *Chandra* data. A similar conclusion was reached by Hutchings et al. (1998) based on analysis of the nuclear spectrum. Thus, this distinct lack of nuclear gas makes 3C 264 rather different from most XBONGs. However, in 3C 264 there is a bright radio nucleus, and the radio and X-ray emissions could be enhanced relative to the optical continuum if the continuum nuclear emission[16] is primarily of a non-thermal origin.

Our data make it clear that the primary radiation mechanism of the 3C 264 jet and nucleus in the radio through ultraviolet is synchrotron emission. A broken power-law synchrotron model (left panel of Figure 13) describes the overall characteristics of the radio-to-optical spectrum of the nucleus rather well, especially given the non-contemporaneous nature of the data. We have assumed a spherical blob of radius 2 pc, in which an electron spectrum of minimum Lorentz factor $\gamma_{\rm min} = 300$ produces radiation of spectral index $\alpha = 0.5$ in a minimum-energy magnetic field of ~ 9 mG, breaking by $\Delta\alpha = 0.7$ at $\gamma_{\rm break} = 7 \times 10^4$ (see, e.g., Worrall & Birkinshaw 2006 for relevant formulae). The dominant X-ray inverse Compton mechanism is synchrotron self-Compton, but this gives a negligible contribution to the observed X-rays. It is interesting that the synchrotron lifetime of electrons producing emission close to the break frequency is ~ 5 yr, of the same order of magnitude as the light-travel time across the source. However, $\Delta\alpha$ is greater than the value of 0.5 expected for a simple energy-loss model, and is in the range 0.6–0.9 commonly found for the resolved jets of low-power radio galaxies, and not yet readily explained by acceleration models (see Worrall 2009 for a review). We return to this latter issue in Section 4.2. While a synchrotron model can describe the overall features of the nuclear continuum of 3C 264, we note that the more extreme case of a radio and X-ray bright (and unabsorbed) radio galaxy with an optically dull continuum, PKS J2310$-$437 (Tananbaum et al. 1997; Worrall et al. 1999), has proved to be more problematic to fit to a simple synchrotron model (Bliss et al. 2009).

Also supporting a synchrotron nature for the nuclear emissions in the optical are the polarized emissions found by our *HST* observations. A similar conclusion was reached by Capetti et al.

---
[16] We note the presence of narrow forbidden lines in the optical spectrum (Hutchings et al. 1998).
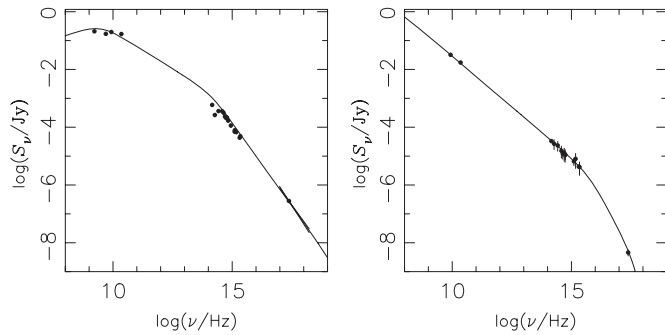
Figure 13. Left panel: spectrum of the nucleus using data from this paper and radio points at 1.66 and 5 GHz from Lara et al. (2004). A simple one-zone synchrotron model (solid line) can describe the overall characteristics of the data as arising from an unresolved small-scale jet. Right panel: spectrum of the outer jet also fitted to a synchrotron model. See the text for details.

(2007), who note an optical polarization ∼8% for the core and a position angle for the electric field vectors ∼5°. This fractional polarization is too high to be reached with scattering (see Capetti et al. for discussion) and is most consistent with synchrotron radiation. It should be noted, however, that the magnetic field orientation seen by Capetti et al. (2007) is somewhat different (by about 25°) from that seen either in the K-band, A-array data we (or Lara et al. 2004) present, and is also different from that seen in most of the VLBI jet (Kharb et al. 2009). Unfortunately, we cannot use our WFPC2 polarimetry data to comment on this latter issue, as the core is saturated.

The optical emissions from the jet have been known to be due to synchrotron radiation for more than a decade (e.g., Baum et al. 1997). Our data allow us to extend this conclusion considerably. Not only do they allow us to place much better constraints on the shape of the jet's optical SED, but they also show that synchrotron radiation is the dominant jet emission mechanism up to X-ray energies. While the X-ray spectrum of the resolved jet is not measured, the emission is undoubtedly of synchrotron origin. X-rays are measured only from the outer jet where contamination from core emission is least, but they arise from a relatively large region. We have modeled this section of jet with a cylinder of radius 20 pc (Lara et al. 2004) and length 550 pc, and used $\gamma_{min} = 300$. Again inverse Compton scattering, including on the cosmic microwave background radiation, gives a negligible contribution to the observed X-ray emission. Again a synchrotron model of a broken power-law fits well the data (right panel of Figure 13). To find a minimum value of $\Delta\alpha$, we allow the break to occur at as low a frequency as possible, but as for the core the value of $\Delta\alpha$ (0.82) is greater than 0.5, and in the range 0.6–0.9 commonly found for the resolved jets of low-power radio galaxies for which the X-ray spectrum is measured. The jet spectral index below the break is $\alpha = 0.7$, the minimum-energy magnetic field is ∼330 μG, and the Lorentz factor of electrons emitting radiation close to the break is $\gamma_{break} = 1.6 \times 10^6$. The synchrotron lifetime of electrons producing radiation at the break frequency (∼140 yr) is again of the same order of magnitude as the light-travel time across the source.

As noted above, the jet of 3C 264 shows rather subtle magnetic field direction changes, both in the optical/UV and radio. The first region where changes are seen to occur are the knot A/B region, which displays a low polarization region in the interknot region between them, that extends northwest along the northern side of knot A as well as northeast along the eastern side of knot B. Twists in the 30°–90° range are seen to the side of this

feature. The low polarization at the knot maximum is likely to be the result of field superposition, and the polarization angle changes may be due to the occurrence of perpendicular and oblique shocks at the location of the knot maxima. A similar pattern of changing position angles in knot C of the 3C 15 jet has, alternatively, been modeled as the superposition of a helical strand of magnetic field on a more ordered field structure. We do not have the angular resolution in our X-ray data to see anything that might be related to the latter feature (as we do in 3C 15), however, a comparison of the two sources and their associated maps reveals some similarity. A second region is seen with significant rotations in the orientation of the magnetic field, namely the knot D region. This region shows low polarization in the jet interior and particularly at the knot maximum, with magnetic field vectors that follow the jet's flux contours downstream. Such a configuration is very similar to some of the knots in the M87 jet, particularly knots D and F. Perlman et al. (1999) modeled those features as shocks that occur within the jet interior, in a stratified jet where the optical/UV emitting particles are also concentrated in the jet interior, while lower energy, radio emitting particles are more evenly distributed through the jet. Such a model can be applied for the most part to these knots as well, with the possible exception that here, we do not have sufficient evidence in our spectral index maps to say that the knots are much more optically bright than the edges, although the α_{RO} map does show that they do have a slightly flatter radio–optical spectrum. Thus, as in the M87 system, the knots in the 3C 264 jet regions are likely to be sites of enhanced in situ particle acceleration.

The nature of the dust ring in 3C 264 and its relationship to the jet is an interesting topic. We see some apparent steepening in the jet's optical spectrum (from $\alpha_O \approx 0.75$ to $\alpha_O \approx 0.9$) near this location, as well as significant changes in polarization in both the optical and radio. These changes include minima in the radio polarization and changes by 20°–40° in the direction of the magnetic field vectors in the optical. The former does not necessarily indicate an interaction between the jet and the dust ring, but rather is more consistent with absorption of jet radiation by the dust within the ring. Moreover, a closer look at Figure 4 reveals that the spectral and polarization changes begin about 0″.1 closer to the nucleus than the inner edge of the ring. In addition, the changes in the direction of the optical polarization vectors are much stronger near the northern edge and continue in the region beyond the ring. This indicates that the spectral and polarization changes are primarily intrinsic to the jet rather than caused by any screening by or interaction with the ring. Thus, we believe that the disk and jet most likely occupy physically distinct regions of the galaxy. A similar conclusion was reached by Martel et al. (2000) on the basis of the continuous distribution of line emission at the location of the disk, with the galaxy subtracted long-slit spectrum of Hutchings et al. (1998) showing no evidence of line emission from the jet itself.

Beyond 1″, the optical polarization is much harder to measure, due to the much lower optical flux. Interestingly, however, where it is measurable, we see an increased optical polarization in this region, as high as 40%, with an orientation slightly different than that seen in the rest of the inner jet, perhaps reflecting the turn toward a more northerly orientation that is seen in the radio flux contours at slightly greater distances (Figures 2, 3, 8 and Lara et al. 2004).

The overall morphology of the radio through X-ray spectrum of the core+jet (Figure 7, bottom right panel), combined with the power-law slope of the optical-to-X-ray spectrum, is most
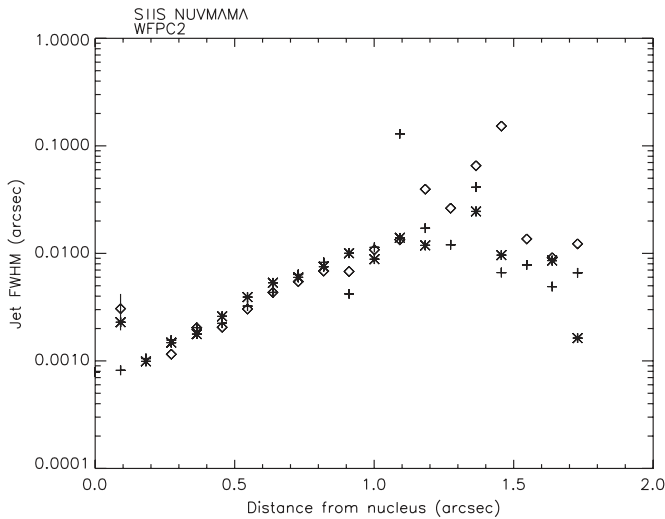
Figure 14. Width of the 3C 264 jet in the UV, optical, and radio. Three data sets were used: the VLA *K*-band, A-array data (crosses), our Stokes I, F555W data (diamonds), and the NUVMAMA image (asterisks). Note the constant rate of increase in jet width, as observed in all three bands out to about 1.′′2 from the core.

consistent with synchrotron radiation. Interestingly, the spectral index observed for the core+inner jet in the X-rays is reasonably similar (within 2σ) to that observed in our data in the ultraviolet for the entire jet, as well as that of the inner jet (the outer jet is too faint to see in the UV data). This implies little curvature of the spectrum between the UV and X-rays, and also implies that the νF_ν peak of the jet's spectrum is located at a few $\times 10^{14}$ Hz, over a broad range of jet components. The spectral break required for the inner 3C 264 jet is $\Delta\alpha = 0.6$; slightly but not significantly smaller than seen in M87 ($\Delta\alpha = 0.7$; Perlman & Wilson 2005). Also in accord with the synchrotron radiation model, we see that the width of the jet is very similar in the radio, optical and UV, for as long as the data allow us to track it (Figure 14). Interestingly, the jet FWHM increases smoothly with distance from the nucleus in all three bands, with the width $W \propto r^{1.1}$ approximately.

4.2. Relationship to Other Jets

It is useful to discuss these results in the broader context of the class of optical and X-ray jets. Ten such jets have now been observed polarimetrically with *HST*: M 87 (Capetti et al. 1997; Perlman et al. 1999), 3C 273 (Thomson et al. 1993), 3C 293 (Floyd et al. 2006), 3C 15, 3C 66B, 3C 78, 3C 264, 3C 346, 3C 371 (Perlman et al. 2006; see also Dulwich et al. 2007, 2009), and most recently PKS 1136−135 (M. Cara et al. 2010, in preparation). Of these the vast majority (all but 3C 273 and PKS 1136−135) are relatively low-power sources, albeit with a variety of optical and radio morphologies. These objects are all at a wide range of distances, ranging from just 16 Mpc in the case of M 87 to $z = 0.534$ in the case of PKS 1136−135. Of these ten, just three (M 87, Perlman et al. 1999; 3C 15 and 3C 346, Dulwich et al. 2007, 2009) have previously had deep analyses of their radio and optical total flux and polarization morphology, as well as broadband spectra and X-ray emission published (importantly, note that the existing *HST* polarimetry of 3C 273 is not deep enough for these purposes). Compared to the other objects, 3C 264's optical and X-ray jet is the most compact: at $2''$ its angular length is less than any other optical/X-ray jet for which polarimetry has been done, except for 3C 78,

which is very similar in length, although its physical length of about 850 pc (projected) is not that much shorter than the 1.5 kpc projected extent of the M87 jet. This limits our ability to extend the detail we can obtain in the radio and optical imagery to the X-rays, as the jet of 3C 264 is only barely resolved with *Chandra*. Thus with these observations we cannot comment in detail on the correlation between changes in optical polarization and the location of X-ray components, previously noted by Perlman & Wilson (2005), Perlman et al. (2006), and Dulwich et al. (2007, 2009).

The dominant polarization configuration observed in the jet of 3C 264, in both the radio and optical, is one of a high polarization (40%–50%) along the jet edges, and somewhat lower polarization in the jet center, with magnetic field vectors oriented primarily along the direction of the jet. Such a configuration is seen in most of the knot A–B complex of the M 87 jet, albeit with considerably more detail because of the greater proximity of that source. What is missing in 3C 264, however (as compared to M87), are the presence of strong "shock-like" components, which are seen not only in the A–B complex of the M 87 jet, but also commonly in the other two jets as well as other regions of the M 87 jet. By contrast, the jet of 3C 264 has a very smooth polarization morphology, unlike any of the other three jets analyzed deeply so far and similar only to 3C 78 in detail. Perhaps related to this, we note that 3C 264 and 3C 78 represent the lowest power jets of those that have been observed polarimetrically with *HST*. It is therefore possible that the overall character of the polarization morphology is partly a function of the jet power. We will test this in our future studies of the remaining jets in the Perlman et al. (2006) sample (3C 78, 3C 371, and 3C 66B, for which future papers are all under preparation).

We turn now to an effect observed in all four jets: the SED peaks at ∼ optical–UV energies, and is followed by a power-law extension, with a break steeper than the canonical $\Delta\alpha = 1/2$. In M87, the spectrum appears to continue to steepen at X-ray energies; however this is not the case in 3C 264. Although a possible formal explanation for this steeper break is that electrons do not diffuse in pitch angle as they radiate (Kardashev 1962; Pacholczyk 1970), a more plausible explanation is that the magnetic field decreases away from the sites of particle acceleration. This naturally results in spectral breaks greater than 1/2, assuming that electrons, after they are accelerated propagate toward regions with lower magnetic field (Wilson 1975). Recent work by Reynolds (2009) has expanded upon this aspect, associating steeper breaks with inhomogeneities and/or differential losses within the source. Another possibility that can work in parallel with the magnetic field gradients is that of velocity gradients in the flow. This idea was first posited by Laing and Bridle (Laing 1996; Bridle 1996) to deal with observed details of radio polarization maps of jets, which suggested a spine-sheath configuration for the jet, with a faster flow in the central spine, similar to a fire hose. Later work invoked lateral velocity gradients to model the sub-pc scale jets of TeV emitting BL Lacertae objects (Georganopoulos & Kazanas 2003), and can be also applied to transverse velocity gradients that may characterize the kpc scale jets of M87 and 3C 264. A velocity gradient across the jet would effectively reduce and/or inhibit a field component in the direction perpendicular to the velocity gradient, and thus would allow for a different polarization morphology in the jet center, as observed here. In this scenario, the high energy emission would come primarily from the fast moving spine, while the low energy emission would be dominated by emission

from the slower sheath (Ghiselini et al. 2005). For small angles $\theta < 1/\Gamma_{sp}$, where Γ_{sp} is the bulk Lorentz factor of the spine, the observed cooling break is the canonical 1/2 break predicted by simple theory. At larger angles, however, the high energy emission of the spine is beamed out of our line of sight more than the sheath emission, and this results in spectral breaks steeper that 1/2 (see Figure 2 of Georganopoulos & Kazanas 2003). It is important to point out that these two possible explanations are not mutually exclusive; indeed, this can be seen by the breadth of work that has developed on the SED of the M87 jet, where the spectrum continues to steepen through the X-rays. This caused Perlman & Wilson (2005) to invoke particle acceleration in an energy-dependent part of the cross section of the jet to explain this, while other authors (Fleishman 2006; Liu & Shen 2007; Sahayanathan 2008) have expanded on this by invoking two-zone, and in one case a diffusive, shock models. Work on other jet sources has expanded upon this by invoking velocity shear and deceleration (NGC 315: Worrall et al. 2007; 3C 31: Laing et al. 2008; see also Wang et al. 2009). In these sources, both toroidal and longitudinal fields are needed to account for details of the polarization morphology at the jet edges. These last two sources are rather similar in flux and polarization morphology to 3C 264, albeit longer and without optical emission from their jets. This is particularly true when the details of the F330W polarization maps (Figure 9) are taken into account. Note, however, that while the work to date suggest that particle acceleration is enhanced in shock-like knots (e.g., Perlman & Wilson 2005), a continuous mode of particle acceleration also appears required for most X-ray jets (see, e.g., Perlman & Wilson 2005; Jester et al. 2001, 2005, 2006; Hardcastle et al. 2003, 2006, 2007).

Another issue is orientation. For M 87, this is reasonably well constrained now, as the superluminal motions (Biretta et al. 1995, 1999; Cheung et al. 2007) seen in its jet restrict the angle to our line of sight to values $\leqslant 18°$ (although n.b., this is in conflict with estimates derived from the observed geometry of the disk and knot A, e.g., Ford et al. 1994). A similarly small viewing angle is seen in the 3C 346 jet, which Dulwich et al. (2009) has constrained to be at an orientation of 14^{+8}_{-7} degrees, before bending $22°$ at an oblique shock several arcseconds down the jet. This value is consistent with earlier VLBI analysis as well (Cotton et al. 1995). By comparison, for 3C 264, modeling suggests an orientation angle as large as $\theta \sim 50°$ (Baum et al. 1997; Lara et al. 1997), based on the jet to counter-jet ratio as well as VLBI and *ROSAT* data. No firm constraints exist on the orientation of the 3C 15 jet, the only other one for which a detailed comparison of radio and optical polarimetry has been published to date (Dulwich et al. 2007). As was argued by Perlman & Wilson (2005) in the case of M87 most of the synchrotron optical and X-ray emission comes from the spine of the jet. If we assume that the high energy emitting spine is also faster than the mostly radio emitting sheath, a result supported by numerical simulations of relativistic jets (Aloy et al. 2003), then for sources at greater angles to the line of sight, as possibly is 3C 264, the high energy emission from the fast spine will be more de-amplified than the slower sheath emission. In this scenario, most of the radio emission comes from the slower sheath, independent of orientation, and this may explain the similar radio polarization of 3C 264 and M 87 as shear due to transverse velocity gradients in the plasma is likely to cause the magnetic field to align with the jet. The difference between highly aligned (e.g., M87) and less-aligned (e.g., 3C 264) sources appears at higher energies. In the case

of highly aligned jets, one expects that the optical and X-ray emission we observe is dominated by the fast spine, where a significant part of the high-energy particle acceleration takes place, most probably in shocks manifested through magnetic field orientations perpendicular to the jet axis—as indeed is seen particularly in the polarization data for the inner knots, e.g., Perlman et al. (1999) and Perlman & Wilson (2005). However, in 3C 264, which is seen at a considerably larger angle, any high-energy emission coming from the fast spine will be de-amplified and thus the X-ray emission we see is most likely originating in the slower sheath. This may explain the fact the optical polarization of 3C 264 is, in general, parallel to the jet axis, following the radio jet polarization pattern. It also suggests that 3C 264 requires a mechanism for distributed particle acceleration, as suggested also for the much more powerful jet of 3C 273 by Jester et al. (2007). This scenario needs testing with optical and radio polarimetry of additional jets.

4.3. Summary

We have presented new VLA, *Chandra*, and *HST* imaging and polarimetric data on the jet of 3C 264 that allow us to make a comprehensive, multi-band study of the energetics and structure of this jet, and the relationship of these factors to the high-energy emission. We present polarization maps in the radio and optical, as well as total flux and spectral index maps in both bands. We also present the first X-ray image of the jet and discuss its relationship to the structure seen in other bands. The dominant emission mechanism of the jet in the X-rays is found to be synchrotron emission. We find significant curvature of the jet spectrum both between the radio and optical and also within the optical–UV band. We present a model of the jet emission that includes a smooth extrapolation of the optical–UV spectrum into the X-ray with a break at particle Lorentz factors $\gamma = 1.6 \times 10^6$ that is steeper than the canonical 0.5. We discuss mechanisms for producing the observed high-energy emission and the anomalously large spectral breaks observed in 3C 264 and M87, and we suggest that it can be due to differential losses, velocity gradients and/or magnetic field gradients coupled with more effective particle acceleration taking place in the faster and/or higher magnetic field parts of the flow. It is, however, important to note that a full test of these mechanisms would require higher angular resolution data than currently available, as *Chandra* barely resolves the jet emission in the X-rays. In the polarization data, we find a smooth yet complex magnetic field structure in the jet which, while without exhibiting sharp, "knotty" structures (as seen in some other high-resolution polarization maps, e.g., M87), displays a structure that is correlated with changes in the optical spectrum. While such a configuration is seen also in other jets, such as M87, here the orientation is rather different, with 3C 264 being at a rather larger angle to our line of sight. Thus, in 3C 264, the spine-sheath configuration manifests itself in the form of more subtle differences between optical and radio polarizations. These include significantly higher polarization at the jet edges, as well as twists in the magnetic field orientation near the positions of two knots and in the interknot regions, seen particularly in the optical polarization data in the knot A/B region and near knot D. Such a configuration is also consistent with the observed SED of 3C 264, but requires a distributed particle acceleration mechanism.

Based on observations made with the NASA/ESA *Hubble Space Telescope*, which is operated by the Association of

REFERENCES

Aloy, M.-A., Marti, J. M., Gomez, J. L., Agudo, I., & Ibanez, J. M. 2003, ApJ, 585, L109

Anderson, J., & King, I. 2003, PASP, 803, 113

Anderson, J., & King, I. 2004, ACS Instrument Science Report, ACS 04-15 (Baltimore, MD: STScI)

Baum, S. A., Heckman, T., & van Breugel, W. 1990, ApJS, 74, 389

Baum, S. A., Heckman, T. M., & van Breugel, W. 1992, ApJ, 389, 208

Baum, S., et al. 1997, ApJ, 483, 178

Baum, S., et al. 1998, ApJ, 492, 854

Biretta, J. A., Sparks, W. B., & Macchetto, F. 1999, ApJ, 520, 621

Biretta, J. A., Zhou, F., & Owen, F. N. 1995, ApJ, 447, 582

Bliss, A. F., Worrall, D. M., Birkinshaw, M., Murray, S. S., & Tananbaum, H. 2009, ApJ, 698, 1061

Bridle, A. H., & Vallee, J. P. 1981, AJ, 86, 1165

Bridle, A. H. 1996, in ASP Conf. Ser. 100, Energy Transport in Radio Galaxies and Quasars, ed. P. E. Hardee, A. H. Bridle, & J. A. Zensus (San Francisco, CA: ASP), 383

Capetti, A., Axon, D. J., Chiaberge, M., Sparks, W. B., Macchetto, F. D., Cracraft, M., & Celotti, A. 2007, A&A, 471, 137

Capetti, A., Macchetto, F. D., Sparks, W. B., & Biretta, J. A. 1997, A&A, 318, 997

Carter, C., Karovska, M., Jerius, D., Glotfelty, K., & Beikman, S. 2003, in ASP Conf. Ser. 295, Astrophysical Data Analysis Software and Systems XII, ed. H. E. Payne, R. I. Jedrzejewski, & R. N. Hook (San Francisco, CA: ASP), 477

Cheung, C. C., Harris, D. E., & Stawarz, L. 2007, ApJ, 663, L65

Civano, F., et al. 2007, A&A, 476, 1223

Cortese, L., Gavazzi, G., Boselli, A., Iglesias-Paramo, J., & Carrasco, L. 2004, A&A, 425, 429

Cotton, W. D., Feretti, L., Giovannini, G., Venturi, T., Lara, L., Marcaide, J., & Wehrle, A. E. 1995, ApJ, 452, 605

Crane, P., et al. 1993, ApJ, 402, L37

Dickenson, M., Mobasher, B., & Roye, E. (ed.) 2004, HST Data Handbook for NICMOS, Version 6.0 (Baltimore, MD: STScI)

Dickey, J. M., & Lockman, F. J. 1990, ARA&A, 28, 215

Donato, D., Sambruna, R. M., & Gliozzi, M. 2004, ApJ, 617, 915

Dulwich, F., Worrall, D. M., Birkinshaw, M., Padgett, C. A., & Perlman, E. S. 2007, MNRAS, 374, 1216

Dulwich, F., Worrall, D. M., Birkinshaw, M., Padgett, C. A., & Perlman, E. S. 2009, MNRAS, 398, 1207

Dunkley, J., et al. 2009, ApJS, 180, 306

Edge, D. O., Shakeshaft, J. R., McAdam, W. B., Baldwin, J. E., & Archer, S. 1959, Mem. R. Astron. Soc., 68, 37

Elvis, M., Schreier, E. J., Tonry, J., Davis, M., & Huchra, J. P. 1981, ApJ, 246, 20

Evans, D. A., Worrall, D. M., Hardcastle, M. J., Kraft, R. P., & Birkinshaw, M. 2006, ApJ, 642, 96

Fanaroff, B. L., & Riley, J. M. 1974, MNRAS, 167, 31

Fleishman, G. D. 2006, MNRAS, 365, L11

Floyd, D. J. E., et al. 2006, ApJ, 639, 23

Ford, H. C., et al. 1994, ApJ, 435, L27

Gavazzi, G., Perola, G. C., & Jaffe, W. 1981, A&A, 103, 35

Georganopoulos, M., & Kazanas, D. 2003, ApJ, 594, L27

Ghisellini, G., Tavecchio, F., & Chiaberge, M. 2005, A&A, 432, 401

Hardcastle, M. J., et al. 2007, ApJ, 670, L81

Hardcastle, M. J., Kraft, R. P., & Worrall, D. M. 2006, MNRAS, 368, L15

Hardcastle, M. J., Worrall, D. M., Kraft, R. P., Forman, W. R., Jones, C., & Murray, S. S. 2003, ApJ, 593, 169

Heyer, I. 2004, WFPC2 Instrument Handbook, Version 9.0 (Baltimore, MD: STScI)

Hutchings, J. B., Baum, S. A., Weistrop, D., Nelson, C., Kaiser, M. E., & Gelderman, R. F. 1998, AJ, 116, 634

Jester, S., Harris, D. E., Marshall, H. L., & Meisenheimer, K. 2006, ApJ, 648, 900

Jester, S., Röser, H.–J., Meisenheimer, K., & Perley, R. 2005, A&A, 431, 477

Jester, S., Röser, H.–J., Meisenheimer, K., Perley, R., & Conway, R. 2001, A&A, 373, 447

Jester, S., et al. 2007, MNRAS, 380, 828

Kardashev, N. S. 1962, Sov. Astron., 6, 317

Kharb, P., Gabuzda, D. C., O'Dea, C. P., Shastri, P., & Baum, S. A. 2009, ApJ, 694, 1485

Laing, R. A. 1996, in ASP Conf. Ser. 100, Energy Transport in Radio Galaxies and Quasars, ed. P. E. Hardee, A. H. Bridle, & J. A. Zensus (San Francisco, CA: ASP), 241

Laing, R. A., Bridle, A. H., Parma, P., Feretti, L., Giovannini, G., Murgia, M., & Perley, R. A. 2008, MNRAS, 386, 657

Lara, L., Cotton, W. D., Feretti, D., Giovannini, G., Venturi, T., & Marcaide, J. M. 1997, ApJ, 474, 179

Lara, L., Feretti, L., Giovannini, G., Baum, S., Cotton, W. D., O'Dea, C. P., & Venturi, T. 1999, ApJ, 513, 197

Lara, L., Giovannini, G., Cotton, W. D., Feretti, L., & Venturi, T. 2004, A&A, 415, 905

Li, J.-Q., Kastner, J. H., Prigozhin, G. Y., Schulz, N. S., Feigelson, E. D., & Getman, K. V. 2004, ApJ, 610, 1204

Lipovka, A. A., Lipovka, N. M., Gosachinskii, I. V., & Chavira, E. 2005, Astron. Zh., 82, 483

Liu, W.-P., & Shen, Z.-Q. 2007, ApJ, 668, L23

Marshall, H. L., et al. 2005, ApJS, 156, 13

Martel, A. R., et al. 1998, ApJ, 496, 203

Martel, A. R., et al. 1999, ApJS, 122, 81

Martel, A. R., Turner, N. J., Sparks, W. B., & Baum, S. A. 2000, ApJS, 130, 267

Noel-Storr, J., Baum, S. A., Verdoes Kleijn, G., van der Marel, R. P., O'Dea, C. P., de Zeeuw, P. T., & Carollo, C. M. 2003, ApJS, 148, 419

Pacholczyk, A. G. 1970, Radio Astrophysics (San Francisco, CA: Freeman)

Pavlovsky, C., et al. 2005, ACS Data Handbook, Version 4.0 (Baltimore, MD: STScI)

Perlman, E. S., Biretta, J. A., Sparks, W. B., Macchetto, F. D., & Leahy, J. P. 2001, ApJ, 551, 206

Perlman, E. S., Biretta, J. A., Zhou, F., Sparks, W. B., & Macchetto, F. D. 1999, AJ, 117, 2185

Perlman, E. S., & Wilson, A. S. 2005, ApJ, 627, 140

Perlman, E. S., et al. 2006, ApJ, 651, 735

Reynolds, S. P. 2009, ApJ, 703, 662

Sahayanathan, S. 2008, MNRAS, 388, L49

Serkowski, K. 1962, in Advances in Astronomy and Astrophysics, Vol. 1, ed. Z. Kopal (New York: Academic Press), 289

Sparks, W. B., Baum, S. A., Biretta, J., Duccio Macchetto, F., & Martel, A. R. 2000, ApJ, 542, 667

Sun, M., Jones, C., Forman, W., Vikhlinin, A., Donahue, M., & Voit, M. 2007, ApJ, 657, 197

Sun, M., Vikhlinin, A., Forman, W., Jones, C., & Murray, S. S. 2005, ApJ, 619, 169

Tananbaum, H., Tucker, W., Prestwich, A., & Remillard, R. 1997, ApJ, 476, 83

Thomson, R. C., Mackay, C. D., & Wright, A. E. 1993, Nature, 365, 133

Tonry, J. L. 1991, ApJ, 373, L1

Wang, Y., Kaiser, C. R., Laing, R. A., Alexander, P., Pavlovski, G., & Knigge, C. 2009, MNRAS, 397, 1113

Wilson, A. S. 1975, A&A, 43, 1

Worrall, D. M. 2009, A&AR, 17, 1

Worrall, D. M., & Birkinshaw, M. 2005, MNRAS, 360, 926

Worrall, D. M., & Birkinshaw, M. 2006, in Lecture Notes in Physics, Vol. 693, Physics of Active Galactic Nuclei at All Scales, ed. D. Alloin, R. Johnson, & P. Lira (Berlin: Springer), 39

Worrall, D. M., Birkinshaw, M., Laing, R. A., Cotton, W. D., & Bridle, A. H. 2007, MNRAS, 380, 2

Worrall, D. M., Birkinshaw, M., Remillard, R. A., Prestwich, A., Tucker, W. H., & Tananbaum, H. 1999, ApJ, 516, 163